DESIGN OF COLD-FORMED HIGH STRENGTH STEEL CHS-to-RHS T- AND X-JOINTS AT ELEVATED TEMPERATURES

Madhup Pandey[1] and Ben Young[2,*]

[1]Department of Civil Engineering, University of Nottingham, Nottingham, United Kingdom.
[2]Department of Civil and Environmental Engineering, The Hong Kong Polytechnic University, Hong Kong, China.

Abstract

The static resistances of cold-formed S900 steel grade tubular T- and X-joints at elevated temperatures have been numerically investigated in this study. Circular hollow sections (CHS) were used as the braces, while square and rectangular hollow sections (SHS and RHS) were used as the chords for both T- and X-joints. In this study, both T- and X-joints were subjected to compression loads. The mechanical properties of cold-formed S900 steel grade hollow section members at elevated temperatures were used to perform the numerical investigation. The static resistances of CHS-to-RHS T- and X-joints were investigated at 400°C, 500°C, 600°C and 1000°C. The finite element models developed and validated by the authors for ambient temperature and post-fire investigations of cold-formed S900 steel grade CHS-to-RHS T- and X-joints were used in this study to perform numerical investigation at elevated temperatures. A comprehensive FE parametric study, including a total of 768 CHS-to-RHS T- and X-joints, was performed in this study using the validated FE models. Both CHS-to-RHS T- and X-joints were failed by chord face failure and a combination of chord face and chord side wall failure mode. The nominal resistances predicted from design rules given in European code and CIDECT, using mechanical properties at elevated temperatures, were compared with the resistances of CHS-to-RHS T- and X-joints at elevated temperatures. It is shown that the predictions from design rules given in European code and CIDECT are quite conservative but unreliable. As a result, economical and reliable design equations are proposed in this study for predicting the resistances of the investigated joints.

Keywords: Cold-formed steel; CHS-to-RHS; Design equations; Elevated temperature; FE analysis; T- and X-joints.

*Corresponding author. (e-mail: ben.young@polyu.edu.hk).

1. Introduction

It is a known fact that bare steel structures are quite sensitive to elevated temperatures (T). Due to considerable degradation of strength and stiffness of steel material at high elevated temperatures, a tubular joint could fail at a load significantly smaller than its resistance at ambient temperature, which could cause a progressive or sudden collapse of the entire structure. The stakeholders of various civil engineering and infrastructure projects around the world are looking for high strength sustainable materials, including cold-formed high strength steel (CFHSS) tubular members. The application of high strength steel (HSS) (in this study refers to steels with yield strengths higher than 460 MPa) tubular members provides many advantages, including superior strength per unit weight, improved toughness and reduced handling costs. The last two decades have seen a significant increase in the production of CFHSS tubular members. Hollow section members up to S1100 steel grade with nominal yield strength equal to 1100 MPa are now available in the market. However, the lack of adequate research work and design recommendations are the primary reasons hampering the widespread use of these materials. Nonetheless, a series of experimental and numerical investigation were carried out by the authors on CFHSS T- and X-joints [1-10]. In addition, Pandey et al. [1,11] proposed economical design rules for predicting the static strengths of cold-formed S900 and S960 steel grades T- and TF-joints at ambient temperature. Furthermore, experimental and numerical investigations were performed by Lan et al. [12,13] on box-section T- and X-joints with steel grades ranging from S460 to S960. However, it is worth noting that all these investigations were carried out at ambient temperature. So far, no study has been performed to investigate the static behaviour of S900 and higher steel grade tubular joints at elevated temperatures.

Feng and Young [14] carried out a numerical investigation on duplex and AISI 304 stainless steel square and rectangular hollow section (SHS and RHS) T- and X-joints using mechanical properties proposed by Chen and Young [15] at elevated temperatures. Using non-linear regression analysis, Dodaran et al. [16] proposed a design formula to predict the resistance of KT-joints at elevated temperatures. Two methods for predicting the ultimate capacities of circular hollow section (CHS) T-joints at elevated temperatures were proposed by Shao et al. [17] by duly investigating the effects of critical geometric parameters. Nassiraei et al. [18] proposed design equations for CHS X-joints at elevated temperatures, where specimens were reinforced with collar plates. Lan and Huang [19] numerically investigated the joint resistances of duplex, austenitic and AISI 304 stainless steel SHS and RHS (here onwards, RHS will also represents SHS) T- and X-joints at elevated temperatures and proposed design equations for their ultimate resistances. Lan et al. [20] numerically studied the static performance of duplex, austenitic and AISI 304 stainless steel RHS K- and N-joints at elevated temperatures. In addition, design rules were also proposed in Ref. [20] using residual yield strengths. Design rules were proposed by applying temperature correction factors on design equations given in CIDECT [21]. Using transient state analysis, Gao et al. [22] studied the structural behaviour of CHS T-joints with collar plates. The residual resistances of concrete-filled CHS T-joints after fire exposures were studied by Gao et al. [23]. The influence of critical geometric parameters on the residual resistances of CHS T-joints at elevated temperatures was studied by Cheng et al. [24]. Chen et al. [25] studied the static performance of CHS T-joints with ring stiffeners at elevated temperatures and finally proposed design equations for predicting the residual resistances of the investigated joints.

Ozyurt et al. [26] numerically investigated the joint resistances of CHS and SHS T-, Y-, X-, K- and N-joints at elevated temperatures. Based on numerical results, reduction factors were then proposed to estimate the residual resistances of the investigated joints. Ozyurt et al. [27] numerically investigated the joint resistances of elliptical hollow section (EHS) T- and X-joints at elevated temperatures. The critical temperature of CHS K-joints was determined using the deformation rate based criterion in He et al. [28]. Compression loaded full-scale CHS T-joints were experimentally and numerically studied at elevated temperatures by Nguyen et al. [29,30]. The residual resistances of impacted CHS T-joints at elevated temperatures were investigated by Yu et al. [31]. The post-fire residual capacities of CHS T-joints were experimentally studied by Jin et al. [32]. Liu et al. [33] performed a numerical parametric study to investigate the static behaviour of CHS T-joints at elevated temperatures. The structural performance of CHS T-joints subjected to blast and fire was experimentally studied by Yu et al. [34]. The technique of artificial neural network was used by Xu et al. [35] to estimate the resistances of CHS T-joints at elevated temperatures. Static performance of CHS T-joint without internal stiffeners was studied by Tan et al. [36] using experimental and numerical methods. It was reported that the joint resistance sharply reduced at high temperatures.

The residual joint resistances of CHS T-joints subjected to brace in-plane bending load were investigated by Fung et al. [37] at elevated temperatures.

In this study, an extensive numerical investigation was performed to investigate the elevated temperature joint resistances ($N_{f,T}$) of S900 steel grade T- and X-joints made of CHS braces and SHS/RHS chords (i.e. CHS-to-RHS). The static performance of CHS-to-RHS T- and X-joints undergoing compression loads was numerically studied at four elevated temperatures, including 400°C, 500°C, 600°C and 1000°C. At present, design rules for resistances of tubular joints at elevated temperatures are not given in any international code and guide. Thus, using mechanical properties at elevated temperatures, the applicability of design rules given in EC3 [38] and CIDECT [21] was evaluated for the investigated joints. Finally, in this study, economical and reliable design rules are proposed for predicting the resistances of cold-formed S900 steel grade CHS-to-RHS T- and X-joints at elevated temperatures.

2. Methodology used in this investigation

The overall methodology used in the numerical investigation is summarised in this section of the paper. The numerical investigation was conducted using ABAQUS [39]. The static resistances of cold-formed S900 steel grade CHS-to-RHS T- and X-joints subjected to compression loads were numerically investigated at 400°C, 500°C, 600°C and 1000°C. In the absence of any experimental investigation on cold-formed S900 steel grade CHS-to-RHS T- and X-joints at elevated temperatures, the numerical investigation in this study was performed using the finite element (FE) models developed and validated by Pandey et al. [1] and Pandey and Young [2] for cold-formed S900 steel grade CHS-to-RHS T- and X-joints at ambient temperature. It is important to note that similar FE models were also successfully used by Pandey and Young [3] to validate the test results of fire exposed (i.e. post-fire) cold-formed S900 steel grade CHS-to-RHS T- and X-joints using post-fire mechanical properties. As natural fires have different temperature vs time curves and also due to substantial cost involved in a fire test, numerical studies are popularly used for such investigations. It is due to these reasons, the FE models of tubular joints validated against ambient temperature test results were used in many numerical studies [14,19,20,26,27,40-52] for their corresponding elevated temperatures investigations.

The numerical investigation in this study was performed using the constitutive stress-strain model proposed by Li and Young [53] for S900 steel grade tubular members at elevated temperatures. The tubular members used in Pandey et al. [1], Pandey and Young [2,3] and Li and Young [53,54] were produced by the identical manufacturer with similar chemical compositions, therefore, the constitutive stress-strain model proposed by Li and Young [53] at elevated temperatures can safely be used in this study. The numerical investigation was then performed using the mechanical properties predicted from the stress-strain model [53] at 400°C, 500°C, 600°C and 1000°C. The stress-strain curves of cold-formed S900 steel grade tubular member obtained from steady state tests for temperatures ranging from 100°C to 1000°C are reported in Li and Young [54]. It should be noted that for temperatures less than 400°C, the deterioration of mechanical properties of cold-formed S900 steel grade tubular member was insignificant. As reported in Li and Young [54], the residual values of ultimate strength of cold-formed S900 steel grade tubular member at 400°C, 500°C, 600°C and 1000°C were 83%, 60%, 35% and 2% of the corresponding ultimate strength at ambient temperature. Therefore, in order to investigate a wide range of strength reductions at elevated temperatures, the numerical investigation in this study was performed at 400°C, 500°C, 600°C and 1000°C.

3. Summary of test programs of cold-formed high strength steel CHS-to-RHS T- and X-joints at ambient temperature and post-fire conditions

The static performances of cold-formed S900 steel grade CHS-to-RHS T- and X-joints were experimentally investigated at ambient temperature by Pandey and Young [55,56]. The braces and chords were welded using metal active gas welding. In total, 8 CHS-to-RHS T-joints [55] and 10 CHS-to-RHS X-joints [56] were tested at ambient temperature. The chord members of CHS-to-RHS T-joint test specimens were simply supported and compression loads were applied via braces. The CHS-to-RHS X-joint test specimens were also subjected to axial compression loads via braces, where top brace end was fixed and bottom brace end only translated vertically with the loading ram. The nominal 0.2% proof stress of tubular members was 900 MPa. In the experimental investigations [55,56], β (d_1/b_0) varied from 0.59 to 0.89, τ (t_1/t_0) varied from 0.66 to 1.00 and 2γ (b_0/t_0) varied from 20.5 to 30.5. The symbols b, h, t and R stand for cross-section width, depth, thickness and external corner radius of RHS member, respectively. The symbol d denotes diameter of CHS member. The subscripts of symbols 0 and 1 denote chord and brace, respectively. Fig. 1 presents various notations for CHS-to-RHS T-joints, which also remain valid for corresponding X-joint counterparts. The failure modes identified in the tests [55,56] were chord face failure (F) and a combination of chord face and chord side wall failure, named combined failure (F+S). The test results were obtained in the form of N vs u and N vs v curves, where N, u and v stand for brace axial static load, chord face indentation and chord side wall deformation, respectively.

The residual static strengths of fire exposed cold-formed S900 steel grade CHS-to-RHS T- and X-joints was experimentally investigated by Pandey and Young [5]. Before conducting the static joint tests, the test specimens were subjected to a total of three fire exposures with preselected post-fire peak temperatures (ψ) equal to 300°C, 550°C and 750°C, respectively. In total, 7 T-joints and 7 X-joints made of CHS braces and RHS chords were fabricated and tested under compression. The test setups and boundary conditions used in the post-fire investigation of CHS-to-RHS T- and X-joints [5] were identical to those used in the corresponding ambient temperature investigations [55,56]. Moreover, the nominal 0.2% proof stress of without fire exposed tubular members was 900 MPa. The braces and chords were welded using robotic metal active gas welding. The test specimens were exposed to fire inside a gas furnace, where the furnace temperature was increased in accordance with the ISO-834 [57]. After attaining the preselected post-fire peak temperatures (ψ), the test specimens were allowed to naturally cool inside the furnace. Subsequently, static tests on CHS-to-RHS T- and X-joints were conducted at ambient temperature. In the tests [5], β varied from 0.74 to 0.89, τ varied from 0.76 to 1.02 and 2γ varied from 25.1 to 30.6. The lengths of braces (L_1) were equal to two times the brace diameter (d_1). On the other hand, the lengths of chords (L_0) were equal to $h_1 + 3h_0 + 180$ mm and $h_1 + 3h_0$ mm for T- and X-joints, respectively [5,55].

4. Numerical programs of cold-formed high strength steel CHS-to-RHS T- and X-joints at ambient temperature and post-fire conditions

4.1. General

The numerical investigations of cold-formed S900 steel grade CHS-to-RHS T- and X-joints at ambient temperature and post-fire conditions were conducted using ABAQUS [39]. The static (general) analysis procedure given in ABAQUS [39] was used as the solver. As the induced strains in the FE model during the applied load were unidirectional (i.e. no load reversal), the isotropic strain hardening law was selected for the analysis. The von-Mises yield criterion is generally the default criterion used to predict the onset of yielding in most metals, except for porous metals. Therefore, the yielding onsets of FE models in this study were based on the von-Mises yield theory. In the FE analyses, the growth of the time step was kept non-linear in order to reduce the overall computation time. Furthermore, the default Newton-Raphson method was used to find the roots of non-linear equilibrium equations. In addition to the accuracy associated with the Newton-Raphson method, one of the other benefits of using this numerical technique is its quadratic convergent approach, which in turn significantly increases the convergence rate of non-linear problems.

The material non-linearities were considered in the FE models developed for ambient temperature and post-fire conditions by assigning the measured values of ambient temperature and post-fire static stress-strain values of flat, corner and curved portions of tubular members. However, experimentally obtained constitutive material curves both at ambient temperature and post-fire conditions were transformed into true stress-strain curves prior to their inclusion in the FE models. On the other hand, the geometric non-linearities in both ambient temperature and post-fire FE models were considered by enabling the non-linear geometry parameter (*NLGEOM) in ABAQUS [39], which allowed FE models to undergo large displacement during the analyses. Furthermore, various parameters, including through-thickness division, contact interactions, mesh seed spacing, corner region extension and element types, were also studied and reported in the following sub-sections of this paper. The labelling of both ambient temperature and post-fire FE specimens was kept identical to the label system used in their corresponding test programs [5,55,56]. Figs. 2 and 3 present illustrations of typical CHS-to-RHS T- and X-joint FE models, respectively.

4.2. Element type, mesh spacing and mechanical properties

Except for the welds, all other parts of both ambient temperature and post-fire FE models were developed using second-order hexahedral elements, particularly using the C3D20 elements. On the other hand, the second-order tetrahedral element, C3D10, was used to model the weld parts due to their complicated shapes. The weld parts were freely meshed using the free-mesh algorithm, however, brace and chord parts were meshed using the structure-mesh algorithm. The use of solid elements helped in making realistic fusions between tubular and weld parts of FE models. Convergence studies were conducted using different mesh sizes, and finally, chord and brace members were seeded at 4 mm and 7 mm intervals, respectively, along their corresponding longitudinal and transverse directions. Moreover, the seeding spacings of weld parts reciprocated the seeding spacings of their respective brace parts. In order to assure the smooth transfer of stresses from flange to web regions, the corner portions of RHS were split into ten elements. FE analyses were also conducted to examine the influence of divisions along the wall thickness (t) of tubular members. The results of these FE analyses demonstrated the trivial influence of wall thickness divisions on the load vs deformation curves of the investigated CHS-to-RHS T- and X-joints. The use of the C3D20 element as well as the small thickness of test specimens [5,55,56] lead to such observations. It is worth noting that similar findings were also obtained in other studies [1,11,58]. Thus, for the validations of both ambient temperature and post-fire FE models, the wall thickness of tubular members was kept undivided. The measured values of ambient temperature and post-fire static stress-strain curves of flat and corner portions of RHS members as well as curved portions of CHS members [4,55] were used in the corresponding FE models. In addition, the influence of cold-working on material properties was included in the FE models by assigning wider corner regions. Various distances for corner extension were considered in the sensitivity analyses, and finally, the corner portions were extended by $2t$ into the neighbouring flat portions, which was in agreement with other studies conducted on CFHSS tubular members and joints [1,11,59-61].

4.3. Weld modelling and contact interactions

The fillet welds were modelled in all FE specimens using the average values of measured weld sizes reported in test programs [5,55,56]. The inclusions of weld geometries appreciably improved the overall accuracies of FE models. In addition, modelling of weld parts helped attain realistic load transfer between brace and chord members, which facilitated in obtaining the actual joint behaviour. The selection of the C3D10 element maintained optimum stiffness around the joint perimeter due to its ability of taking complicated shapes. In total, two types of contact interactions were defined for CHS-to-RHS T- and X-joints FE models. First, contact interaction between brace and chord members of CHS-to-RHS T- and X-joints FE models. Second, contact interaction between chord members and chord end bearing blocks of CHS-to-RHS T-joint FE models. Both contact interactions were established using the built-in surface-to-surface contact definition. In addition, a tie constraint was also established between weld and tubular members of CHS-to-RHS T- and X-joints FE models. The contact interactions between brace and chord members of CHS-to-RHS T- and X-joints FE models was kept frictionless, while a frictional penalty equal to 0.3 was imposed on the contact interaction between chord member and chord end bearing blocks of CHS-to-RHS T-joint FE models. Along the normal direction of these two contact interactions, a 'hard' contact pressure overclosure was used. In addition, finite sliding was permitted between the interaction surfaces. For contact interactions and tie constraint, the surfaces were connected to each other using the 'master-slave' algorithm technique. This technique permits the separation of fused surfaces under tension, however, it does not allow penetration of fused surfaces under compression. For brace-to-chord contact interaction of CHS-to-RHS T- and X-joints, the cross-section surface of brace connected to chord member was assigned as the 'master' region (relatively less deformable), while chord connecting surface(s) was assigned as the 'slave' region (relatively more deformable), as shown in Fig. 4(a). Similarly, for chord-to-bearing block contact interaction of CHS-to-RHS T-joint, bearing blocks were assigned as the 'master' region, while chord was assigned as the 'slave' region, as shown in Fig. 4(b). On the other hand, for weld-tubular member tie connection, the weld surfaces were assigned as the 'master' regions, while the connecting brace and chord surfaces were assigned as the 'slave' regions, as shown in Fig. 5.

4.4. Boundary conditions and load application

The boundary conditions in CHS-to-RHS T- and X-joints FE models were assigned by creating reference points. Three reference points were created for the CHS-to-RHS T-joint FE model, including one top reference point (TRP) and two bottom reference points (BRP-1 and BRP-2). The TRP replicated the fixed boundary condition of the top brace end, while BRP-1 and BRP-2 replicated the boundary conditions of roller positioned at each chord end. As shown in Fig. 2, the TRP was created at the cross-section centre of the top brace end, while BRP-1 and BRP-2 were created at 20 mm below the centre of the bottom surfaces of chord end bearing blocks. The TRP, BRP-1 and BRP-2 were then coupled to their corresponding surfaces using the built-in kinematic coupling type. In order to exactly replicate the boundary conditions of the CHS-to-RHS T-joint test setup, all degrees of freedom (DOF) of TRP were restrained. On the other hand, for BRP-1 and BRP-2, except for the translations along the vertical and longitudinal directions of the CHS-to-RHS T-joint FE specimen as well as the rotation about the transverse direction of the chord member, all other DOF of BRP-1 and BRP-2 were also restrained. In addition, all DOF of other nodes of CHS-to-RHS T-joint FE specimen were kept unrestrained for both rotation and translation.

For CHS-to-RHS X-joint FE model, the top and bottom reference points (TRP and BRP) were created at the cross-section centres of the top and bottom brace members, as shown in Fig. 3. Subsequently, TRP and BRP were coupled to their respective brace end cross-section surfaces using the kinematic coupling type. In order to exactly replicate the boundary conditions of the CHS-to-RHS X-joint test setup, all DOF of TRP were restrained. However, except for the translation along the vertical direction of the CHS-to-RHS X-joint specimen, all other DOF of BRP were also restrained. Moreover, all DOF of other nodes of the CHS-to-RHS X-joint FE specimen were kept unrestrained for both rotation and translation. Using the displacement control method, compression load was then applied at the bottom reference points of the CHS-to-RHS T- and X-joints FE specimens. In addition, the size of the step increment was kept small in order to obtain smooth load vs deformation curves. Following this approach, the boundary conditions and load applications in FE models were identical to those used in the test programs [5,55,56].

4.5. FE validations of CHS-to-RHS T- and X-joints at ambient temperature and post-fire conditions

The FE models of cold-formed S900 steel grade CHS-to-RHS T- and X-joints at ambient temperature [1,2] and post-fire conditions [3] were developed using the modelling techniques described in the preceding sub-sections of this paper. The validations of FE models were confirmed by duly comparing the joint resistances, load vs deformation curves and failure modes between tests [5,55,56] and their corresponding FE [1-3] specimens. The measured dimensions of tubular members and welds were used to develop all FE models. In addition, measured ambient temperature and post-fire static mechanical properties were used in the validations of corresponding ambient temperature and post-fire FE models. It is worth mentioning that for both ambient temperature and post-fire investigations, the peak load or 3% deformation limit load, whichever occurred earlier in the N vs u curve, was taken as the joint resistance [21]. For the ambient temperature investigation of cold-formed S900 steel grade CHS-to-RHS T-joints, the overall values of the mean (P_m) and coefficients of variation (COV) (V_p) of the comparisons between test and FE resistances were 1.02 and 0.018, respectively [1]. Similarly, for cold-formed S900 steel grade CHS-to-RHS X-joints at ambient temperature, the overall values of P_m and V_p of the comparisons between test and FE resistances were 1.01 and 0.020, respectively [2]. Besides, on using the similar FE models with post-fire static mechanical properties, the overall values of P_m of the comparisons between post-fire test and FE resistances of cold-formed S900 steel grade CHS-to-RHS T- and X-joints were 1.02 and 0.99, respectively [3]. On the other hand, the overall values of V_p of these comparisons were 0.009 and 0.007 for CHS-to-RHS T- and X-joints, respectively [3]. In addition, the comparisons of load vs deformation curves between test and FE CHS-to-RHS T- and X-joint specimens for ambient temperature are shown in Figs. 6 and 7, respectively. However, the comparisons of load vs deformation curves between test and FE CHS-to-RHS T- and X-joint specimens for post-fire conditions are shown in Figs. 8 and 9, respectively. Furthermore, Figs. 10 and 11 present comparisons of failure modes between test and FE CHS-to-RHS T- and X-joint specimens for ambient temperature investigation, respectively. On the other hand, the comparisons of failure modes between test and FE CHS-to-RHS T- and X-joint specimens for post-fire investigation are shown in Figs. 12 and 13, respectively. Hence, it can be concluded that the verified FE models precisely replicated the overall static behaviour of cold-formed S900 steel grade CHS-to-RHS T- and X-joints for both ambient temperature and post-fire investigations.

5. Numerical investigation of cold-formed high strength steel CHS-to-RHS T- and X-joints at elevated temperatures

5.1. FE parametric study

The numerical investigation of cold-formed S900 steel grade CHS-to-RHS T- and X-joints at elevated temperatures was performed using the FE method. The FE models developed and validated by Pandey et al. [1] and Pandey and Young [2,3] for ambient temperature and post-fire investigations, respectively, were used to perform numerical study in this investigation. A detailed parametric study was performed in the numerical investigation at four elevated temperatures, including 400°C, 500°C, 600°C and 1000°C. The mechanical properties of cold-formed S900 steel grade tubular members at elevated temperatures were predicted using the constitutive material model proposed by Li and Young [53] and subsequently adopted in ABAQUS [39] for numerical investigation. Fig. 14 presents the stress-strain curves at 400°C, 500°C, 600°C and 1000°C. Table 1 presents the mechanical properties at 400°C, 500°C, 600°C and 1000°C, which include Young's modulus (E_0), 0.2% proof stress ($\sigma_{0.2}$), ultimate strength (σ_u) and ultimate strain (ε_u). With the exception of at elevated temperatures, all FE modelling techniques described in Section 4 of this paper were used to perform the numerical parametric study on cold-formed S900 steel grade CHS-to-RHS T- and X-joints at elevated temperatures.

In order to gain a broad understanding of various critical factors affecting the static behaviour of CHS-to-RHS T- and X-joints at elevated temperatures, the database was widened by performing a comprehensive numerical parametric study. In total, 768 FE analyses were performed in the parametric study, including 384 CHS-to-RHS T-joints and 384 CHS-to-RHS X-joints. The validity ranges of important geometric parameters were purposefully widened beyond the present limitations set by EC3 [38] and CIDECT [21]. Table 2 presents the overall ranges of various critical parameters considered in this investigation. In the parametric study, the diameter of CHS braces varied from 15 mm to 450 mm, while the values of cross-section width and depth of RHS chords of parametric FE specimens varied from 50 mm to 500 mm. However, the values of wall thickness of braces and chords varied from 2 mm to 10 mm. The external corner radius of RHS member (R_0) conformed to commercially produced HSS members [62]. In this study, R_0 was kept as $2t$ for $t \leq 6$ mm, $2.5t$ for $6 < t \leq 10$ mm and $3t$ for $t > 10$ mm, which in turn also met the limits detailed in EN [63]. The lengths of braces and chords of CHS-to-RHS T- and X-joints FE specimens were determined using the identical formulae used for the test specimens [5,55].

For meshing along the longitudinal and transverse directions of RHS members, seedings were approximately spaced at the minimum of $b/30$ and $h/30$. On the other hand, CHS brace members were meshed approximately at an interval of $d/30$. Overall, the adopted mesh sizes of parametric FE specimens varied from 3 mm to 12 mm. On the other hand, the seeding interval of weld parts of parametric FE specimens reciprocated the seeding interval of their corresponding brace parts. Following the prequalified tubular joint details given in AWS D1.1M [64], the leg size (w) of the fillet weld of CHS-to-RHS T- and X-joints FE specimens was designed as 1.5 times the minimum of t_1 and t_0, which was consistent with the values adopted in the test programs [5,55,56]. For precise replication of RHS curvatures, the corner portions of RHS members were split into ten parts. For tubular members with $t \leq 6$ mm, no divisions were made along the wall thickness of the FE specimens. However, when $t > 6$ mm, the wall thickness of FE specimens was divided into two layers. The weld parts were also assigned the mechanical properties determined from the constitutive material model proposed by Li and Young [53].

5.2. Failure modes

Overall, two types of failure modes were identified in this numerical investigation for both CHS-to-RHS T- and X-joints. First, the failure of CHS-to-RHS T- and X-joints by the yielding of chord flange, which was named as chord face failure and denoted by the letter ‘F’ in this study. Second, the failure of CHS-to-RHS T- and X-joints due to the combination of chord face and chord side wall failure modes, which was termed as the combined failure mode and denoted by ‘F+S’ in this study. Figs. 15 and 16 present chord face failure and combined failure modes of typical CHS-to-RHS T- and X-joints at elevated temperature (500°C), respectively. It is important to note that these failure modes were defined corresponding to the $N_{f,T}$, which in turn was computed by combinedly considering the peak and $0.03b_0$ limit loads, whichever occurred earlier in the $N_{f,T}$ vs u curve [21]. The CHS-to-RHS T- and X-joints were failed by the F mode, when the $N_{f,T}$ was determined using the $0.03b_0$ limit criterion. The applied load in CHS-to-RHS T- and X-joints failed by the F mode was monotonically increasing. In this investigation, CHS-to-RHS T- and X-joints were failed by the F mode when $0.30 \leq \beta \leq 0.70$. For CHS-to-RHS T- and X-joints that failed by the F+S mode, the $N_{f,T}$ vs u curve exhibited a clear ultimate load. Additionally, evident deformations of chord flange, chord webs and chord corner regions were noticed in the specimens that failed by the F+S mode. The specimens were failed by the F+S mode in this investigation when $0.75 \leq \beta \leq 0.90$. Moreover, none of the specimens was failed by the global buckling of braces. Figs. 17 and 18 present the variations of $N_{f,T}$ vs u curves for typical CHS-to-RHS T- and X-joints that failed by the F and F+S failure modes corresponding to the four investigated elevated temperatures, respectively.

6. Design rules

Design rules for predicting the residual strengths of tubular joints at elevated temperatures are currently not given in international codes and guides. In order to examine the suitability of EC3 [38] and CIDECT [21] design provisions for cold-formed S900 steel grade CHS-to-RHS T- and X-joints at elevated temperatures, in this study, the nominal resistances from design equations given in EC3 [38] and CIDECT [21] ($N_{E,T}$ and $N_{C,T}$) were determined using mechanical properties shown in Table 1. The design rules given in EC3 [38] and CIDECT [21] are shown below:

Chord face failure ($\beta \leq 0.85$)

EC3 [38]:

$$N_{E,T} = C_f \left[\frac{\pi}{4} k_n \frac{f_{y0,T} t_0^2}{(1-\beta)\sin\theta_1} \left(\frac{2\eta}{\sin\theta_1} + 4\sqrt{1-\beta} \right) / \gamma_{M5} \right] \tag{1}$$

CIDECT [21]:

$$N_{C,T} = C_f \left[\frac{\pi}{4} Q_f \frac{f_{y0,T} t_0^2}{\sin\theta_1} \left(\frac{2\eta}{(1-\beta)\sin\theta_1} + \frac{4}{\sqrt{1-\beta}} \right) \right] \tag{2}$$

Chord side wall failure ($\beta = 1.0$)

EC3 [38]:

$$N_{E,T} = C_f \left[\frac{\pi}{4} k_n \frac{f_{b,T} t_0}{\sin \theta_1} \left(\frac{2h_1}{\sin \theta_1} + 10t_0 \right) / \gamma_{M5} \right] \quad (3)$$

CIDECT [21]:

$$N_{C,T} = C_f \left[\frac{\pi}{4} Q_f \frac{f_{k,T} t_0}{\sin \theta_1} \left(\frac{2h_1}{\sin \theta_1} + 10t_0 \right) \right] \quad (4)$$

The nominal resistances from EC3 [38] were determined using the 0.2% proof stress at elevated temperatures and partial safety factor (γ_{M5}) equal to 1.0. In addition, a material factor (C_f) equal to 0.80 was adopted as per EC3 [65]. On the other hand, CIDECT [21] uses the minimum of 0.2% proof stress and 0.80 times the corresponding ultimate strength for joint resistance calculation. Moreover, design provisions given in CIDECT [21] recommend the use of C_f equal to 0.90 for tubular joints with steel grade exceeding S355. Unlike EC3 [38], CIDECT [21] uses different values of partial safety factors (γ_M) for different tubular joints and their corresponding failure modes, which are given in IIW [66]. However, their effects are implicitly included inside the CIDECT [21] design provisions. In this study, nominal resistances of CHS-to-RHS X-joints from design equations given in CIDECT [21] were calculated using γ_M equal to 1.0 and 1.25 for chord face failure and chord side wall failure modes, respectively. On the other hand, nominal resistances of CHS-to-RHS T-joints from design equations given in CIDECT [21] were calculated using γ_M equal to 1.0 for both chord face failure and chord side wall failure modes. In Eqs. (1) to (4), chord stress functions are denoted by k_n and Q_f, yield stress of chord member at elevated temperatures is denoted by $f_{y0,T}$, the parameter η is equal to d_1/b_0, chord side wall buckling stresses at elevated temperatures are denoted by $f_{b,T}$ and $f_{k,T}$, and the angle between brace and chord is denoted by θ_1 (in degrees). For CHS-to-RHS T-joints, the effect of chord-in-plane bending was considered through k_n and Q_f functions. However, for CHS-to-RHS X-joints, the values of k_n and Q_f were adopted as 1.0.

In addition, a reliability analysis was performed as per AISI S100 [67]. In this study, design equation was treated as reliable when the value of reliability index (β_0) was greater than or equal to 2.50. The values of various statistical parameters and load combinations used in the reliability index calculation are identical to those values adopted in Pandey et al. [1].

7. Comparisons of joint resistances at elevated temperatures with nominal resistances

Tables 3 and 4 present the overall summary of comparisons between $N_{f,T}$ and nominal resistances predicted from design equations given in EC3 [38] and CIDECT [21] for CHS-to-RHS T-joints failed by the F and F+S failure modes, respectively. On the other hand, Tables 5 and 6 present the overall summary of comparisons between $N_{f,T}$ and nominal resistances predicted from design equations given in EC3 [38] and CIDECT [21] for CHS-to-RHS X-joints failed by the F and F+S failure modes, respectively. The comparisons are also graphically shown in Figs. 19 and 20 for CHS-to-RHS T-joints, and in Figs. 21 and 22 for CHS-to-RHS X-joints.

Table 3 presents the overall summary of comparisons for CHS-to-RHS T-joints that failed by the F mode. The comparison results proved that using the mechanical properties at elevated temperatures, the design rules given in EC3 [38] and CIDECT [21] are slightly conservative but largely scattered and unreliable for the design of S900 steel CHS-to-RHS T-joints at elevated temperatures. For CHS-to-RHS T-joints that failed by the F+S mode, the design rules given in EC3 [38] and CIDECT [21] are found to be very conservative but unreliable, as shown in Table 4. Furthermore, on using the mechanical properties at elevated temperatures, the predictions from design equations given in EC3 [38] and CIDECT [21] are quite dispersed. The overall summaries of comparisons for CHS-to-RHS X-joints failed by the F and F+S modes are shown in Tables 5 and 6. The general trend of comparison results of CHS-to-RHS X-joints failed by F and F+S failure modes are similar to those observed for CHS-to-RHS T-joints failed by F and F+S failure modes, respectively.

In Figs. 19 and 21, generally, CHS-to-RHS T- and X-joints with small values of β and η ratios and large values of 2γ ratio lie below the unit slope line (i.e. $y=x$). For such specimens, the joint resistance corresponding to the $0.03b_0$ limit was not sufficient to cause the yielding of chord flanges. On the contrary, the yield line theory was used to derive the existing design equation for RHS T- and X-joints that failed by the F mode [21,38]. Consequently, the $N_{f,T}$ of CHS-to-RHS T- and X-joints that failed by the F mode became smaller than the corresponding nominal resistances predicted from design equations given in EC3 [38] and CIDECT [21] using mechanical properties at elevated temperatures. As a result, the data of such specimens fall below the line of unit slope. The data above the line of unit slope, on the other hand, indicate CHS-to-RHS T- and X-joints specimens with medium to large values of β and η ratios and small values of 2γ ratio. For CHS-to-RHS T- and X-joints that failed by the F+S mode, the data above the unit slope line in Figs. 20 and 22 typically represent specimens with large values of β ratio and small values of 2γ and h_0/t_0 ratios. As the β ratio of CHS-to-RHS T- and X-joints failed by the F+S mode increased, the brace member gradually approached the chord corner regions. Consequently, the $N_{f,T}$ of such T- and X-joints increased due to the enhanced rigidity of chord corner regions. On the other hand, the corresponding increase in nominal resistances predicted from design equations given in EC3 [38] and CIDECT [21] using mechanical properties at elevated temperatures was lower than the $N_{f,T}$ of CHS-to-RHS T- and X-joints. Subsequently, the data of such specimens fall above the line of unit slope in Figs. 20 and 22.

8. Proposed design rules

Using two design methods, named as proposal-1 and -2, design rules are proposed in this study for different failure modes of the investigated CHS-to-RHS T- and X-joints at elevated temperatures (T). For CHS-to-RHS T-joints, the design rules proposed in both the approaches (i.e. proposal-1 and -2) are based on the design equations proposed by Pandey et al. [1] for cold-formed S900 steel grade CHS-to-RHS T-joints at ambient temperature. On the other hand, for CHS-to-RHS X-joints, the proposed design rules under proposal-1 and -2 are based on the design equations proposed by Pandey and Young [2] for cold-formed S900 steel grade CHS-to-RHS X-joints at ambient temperature. In the first design method (i.e. proposal-1), mechanical properties at ambient temperature used in the design equations proposed by Pandey et al. [1] and Pandey and Young [2] are replaced with the mechanical properties at elevated temperatures. In addition, a correction factor (Ω) based on the elevated temperatures is also applied on the proposed design rules. On the other hand, in the second design method (i.e. proposal-2), only a correction factor (Ω) based on the elevated temperatures is applied on the design rules proposed by Pandey et al. [1] and Pandey and Young [2] for ambient temperature condition. Therefore, design equations under proposal-1 can predict the $N_{f,T}$ of CHS-to-RHS T- and X-joints when mechanical properties at elevated temperatures are available. However, design equations under proposal-2 can predict the $N_{f,T}$ only using the value of elevated temperatures. It should be noted that the design rules proposed in this study are valid for 400°C ≤ T ≤ 1000°C. Furthermore, the validity ranges of important geometric parameters influencing the static behaviour of CHS-to-RHS T- and X-joints were extended beyond their existing limits given in EC3 [38] and CIDECT [21]. Moreover, as welds were modelled in all FE specimens, the influence of welds was implicitly included in the proposed design rules. In order to obtain design resistances (N_d), the proposed nominal resistances (N_{pn1} and N_{pn2}) in the following sub-sections of this paper shall be multiplied by their correspondingly recommended resistance factors (ϕ), i.e. $N_d = \phi$ (N_{pn1} or N_{pn2}).

8.1. CHS-to-RHS T-joints failed by F mode ($0.30 \le \beta \le 0.70$)

The design equations proposed under proposal-1 and -2 for CHS-to-RHS T-joints failed by the F mode at elevated temperatures are as follows:

<u>Proposal-1:</u>

Using mechanical properties at elevated temperatures (T):

$$N_{pn1} = \left(0.54e^{0.0015T}\right)\left[f_{y0,T}t_0^2\left(\frac{1.2e^{3.1\beta}}{0.6+0.025(2\gamma)}\right)\right] \tag{5}$$

<u>Proposal-2:</u>

Using mechanical properties at ambient temperature and elevated temperature correction factor (Ω):

$$N_{pn2} = \Omega\left[f_{y0}t_0^2\left(\frac{1.2e^{3.1\beta}}{0.6+0.025(2\gamma)}\right)\right] \tag{6}$$

where

$$\Omega = \begin{cases} 1.61 - 2\times10^{-3}T & \text{for} \quad 400°\text{C} \le T \le 600°\text{C} \\ 0.95 - 9\times10^{-4}T & \text{for} \quad 600°\text{C} < T \le 1000°\text{C} \end{cases} \tag{7}$$

The Eqs. (5) and (6) are valid for $0.30 \le \beta \le 0.70$, $16.6 \le 2\gamma \le 50$, $16.6 \le h_0/t_0 \le 50$ and $0.50 \le \tau \le 0.90$. As shown in Table 3, the P_m and V_p of proposal-1 (i.e. Eq. (5)) are 1.01 and 0.137, respectively, while the P_m and V_p of proposal-2 (i.e. Eq. (6)) are 1.03 and 0.126, respectively. For both Eqs. (5) and (6), ϕ equal to 0.80 is recommended, resulting in β_0 equal to 2.58 and 2.70, respectively. Thus, both Eqs. (5) and (6) must be multiplied by ϕ equal to 0.80 to obtain their corresponding design resistances (N_d), respectively. The comparisons of $N_{f,T}$ of CHS-to-RHS T-joint specimens with nominal resistances predicted from design equations given in EC3 [38], CIDECT [21] as well as predictions from proposal-1 and -2 are graphically presented in Fig. 19. Compared to the design provisions given in EC3 [38] and CIDECT [21], the Eqs. (5) and (6) are relatively more accurate, less scattered and reliable.

8.2. CHS-to-RHS T-joints failed by F+S mode ($0.75 \leq \beta \leq 0.90$)

The design equations proposed under proposal-1 and -2 for CHS-to-RHS T-joints failed by the F+S mode at elevated temperatures are as follows:

Proposal-1:

Using mechanical properties at elevated temperatures (T):

$$N_{pn1} = \left(0.6e^{0.001T}\right)\left[f_{y0,T}t_0^2\left(\frac{57\beta-30}{0.8+0.013(2\gamma)}\right)\right] \tag{8}$$

Proposal-2:

Using mechanical properties at ambient temperature and elevated temperature correction factor (Ω):

$$N_{pn2} = \Omega\left[f_{y0}t_0^2\left(\frac{57\beta-30}{0.8+0.013(2\gamma)}\right)\right] \tag{9}$$

where

$$\Omega = \begin{cases} 1.67-2.2\times10^{-3}T & \text{for} \quad 400°\text{C} \leq T \leq 600°\text{C} \\ 0.83-8\times10^{-4}T & \text{for} \quad 600°\text{C} < T \leq 1000°\text{C} \end{cases} \tag{10}$$

The Eqs. (8) and (9) are valid for $0.75 \leq \beta \leq 0.90$, $16.6 \leq 2\gamma \leq 50$, $16.6 \leq h_0/t_0 \leq 50$ and $\tau = 1.0$. As shown in Table 4, the P_m and V_p of proposal-1 (i.e. Eq. (8)) are 1.01 and 0.149, respectively, while the P_m and V_p of proposal-2 (i.e. Eq. (9)) are 1.01 and 0.141, respectively. For both Eqs. (8) and (9), ϕ equal to 0.80 is recommended, resulting in β_0 equal to 2.53 and 2.58, respectively. Thus, both Eqs. (8) and (9) must be multiplied by ϕ equal to 0.80 to obtain their corresponding design resistances (N_d), respectively. The comparisons of $N_{f,T}$ of CHS-to-RHS T-joint specimens with nominal resistances predicted from design equations given in EC3 [38], CIDECT [21] as well as predictions from proposal-1 and -2 are graphically presented in Fig. 20. Compared to the design provisions given in EC3 [38] and CIDECT [21], the Eqs. (8) and (9) are relatively more accurate, less scattered and reliable.

8.3. CHS-to-RHS X-joints failed by F mode ($0.30 \leq \beta \leq 0.70$)

The design equations proposed under proposal-1 and -2 for CHS-to-RHS X-joints failed by the F mode at elevated temperatures are as follows:

Proposal-1:

Using mechanical properties at elevated temperatures (T):

$$N_{pn1} = \left(0.61e^{0.0012T}\right)\left[f_{y0,T}t_0^2\left(\frac{1.5e^{3\beta}}{0.65+0.025(2\gamma)}\right)\right] \tag{11}$$

Proposal-2:

Using mechanical properties at ambient temperature and elevated temperature correction factor (Ω):

$$N_{pn2} = \Omega\left[f_{y0}t_0^2\left(\frac{1.5e^{3\beta}}{0.65+0.025(2\gamma)}\right)\right] \tag{12}$$

where

$$\Omega = \begin{cases} 1.66 - 2.1\times10^{-3}T & \text{for} \quad 400°\text{C} \leq T \leq 600°\text{C} \\ 0.94 - 9\times10^{-4}T & \text{for} \quad 600°\text{C} < T \leq 1000°\text{C} \end{cases} \tag{13}$$

The Eqs. (11) and (12) are valid for $0.30 \leq \beta \leq 0.70$, $16.6 \leq 2\gamma \leq 50$, $16.6 \leq h_0/t_0 \leq 50$ and $0.50 \leq \tau \leq 0.90$. As shown in Table 5, the P_m and V_p of proposal-1 (i.e. Eq. (11)) are 1.00 and 0.183, respectively, while the P_m and V_p of proposal-2 (i.e. Eq. (12)) are 1.02 and 0.182, respectively. For both Eqs. (11) and (12), ϕ equal to 0.75 is recommended, resulting in β_0 equal to 2.56 and 2.62, respectively. Thus, both Eqs. (11) and (12) must be multiplied by ϕ equal to 0.75 to obtain their corresponding design resistances (N_d), respectively. The comparisons of $N_{f,T}$ of CHS-to-RHS X-joint specimens with nominal resistances predicted from design equations given in EC3 [38], CIDECT [21] as well as predictions from proposal-1 and -2 are graphically presented in Fig. 21. Compared to the design provisions given in EC3 [38] and CIDECT [21], the Eqs. (11) and (12) are relatively more accurate, less scattered and reliable.

8.4. CHS-to-RHS X-joints failed by F+S mode ($0.75 \leq \beta \leq 0.90$)

The design equations proposed under proposal-1 and -2 for CHS-to-RHS X-joints failed by the F+S mode at elevated temperatures are as follows:

Proposal-1:

Using mechanical properties at elevated temperatures (T):

$$N_{pn1} = \left(0.62e^{0.001T}\right)\left[f_{y0,T}t_0^2 \left(\frac{65\beta - 35}{0.75 + 0.015(2\gamma)} \right) \right] \tag{14}$$

Proposal-2:

Using mechanical properties at ambient temperature and elevated temperature correction factor (Ω):

$$N_{pn2} = \Omega \left[f_{y0}t_0^2 \left(\frac{65\beta - 35}{0.75 + 0.015(2\gamma)} \right) \right] \tag{15}$$

where

$$\Omega = \begin{bmatrix} 1.75 - 2.3\times10^{-3}T & \text{for} & 400°\text{C} \le T \le 600°\text{C} \\ 0.88 - 8.5\times10^{-4}T & \text{for} & 600°\text{C} < T \le 1000°\text{C} \end{bmatrix} \tag{16}$$

The Eqs. (14) and (15) are valid for $0.75 \le \beta \le 0.90$, $16.6 \le 2\gamma \le 50$, $16.6 \le h_0/t_0 \le 50$ and $\tau = 1.0$. As shown in Table 6, the P_m and V_p of proposal-1 (i.e. Eq. (14)) are 1.02 and 0.109, respectively, while the P_m and V_p of proposal-2 (i.e. Eq. (15)) are 1.02 and 0.108, respectively. For both Eqs. (14) and (15), ϕ equal to 0.85 is recommended, resulting in β_0 equal to 2.53. Thus, both Eqs. (14) and (15) must be multiplied by ϕ equal to 0.85 to obtain their corresponding design resistances (N_d), respectively. The comparisons of $N_{f,T}$ of CHS-to-RHS X-joint specimens with nominal resistances predicted from design equations given in EC3 [38], CIDECT [21] as well as predictions from proposal-1 and -2 are graphically presented in Fig. 22. Compared to the design provisions given in EC3 [38] and CIDECT [21], the Eqs. (14) and (15) are relatively more accurate, less scattered and reliable.

It is important to note that for CHS-to-RHS T- and X-joints with $0.70 < \beta < 0.75$, the nominal resistances under proposal-1 can be obtained by performing a linear interpolation between Eqs. (5) & (8) and Eqs. (11) & (14), respectively. Similarly, for proposal-2, the nominal resistances of CHS-to-RHS T- and X-joints with $0.70 < \beta < 0.75$ can be obtained by performing a linear interpolation between Eqs. (6) & (9) and Eqs. (12) & (15), respectively.

9. Conclusions

This paper presents a comprehensive numerical study that investigated the static behaviour of cold-formed S900 steel grade T- and X-joints at elevated temperatures (*T*). Both T- and X-joints had circular hollow section (CHS) braces and square and rectangular hollow section (SHS and RHS) chords. The resistances of CHS-to-RHS T- and X-joints undergoing axial compression loads were determined at 400°C, 500°C, 600°C and 1000°C. The parametric study comprising 768 CHS-to-RHS T- and X-joints was performed using the finite element (FE) models developed and validated by Pandey et al. [1] and Pandey and Young [2,3]. The ranges of governing geometric parameters of FE specimens in the parametric study exceeded the limits prescribed by EC3 [38] and CIDECT [21]. The mechanical properties predicted from constitutive stress-strain model proposed by Li and Young [53] at elevated temperatures were used in the numerical investigation.

All parts of the FE specimens were modelled using the second-order solid elements, which in turn ensured proper fusion between different connecting surfaces and realistic load transfer between braces and chords. Overall, CHS-to-RHS T- and X-joints specimens were failed by chord face failure (F) mode and a combination of chord face failure and chord side wall failure modes, i.e. combined failure (F+S) mode. The nominal resistances predicted from design rules given in EC3 [38] and CIDECT [21], using mechanical properties at elevated temperatures, were compared with the resistances of the investigated CHS-to-RHS T- and X-joints. It is shown that the design rules given in EC3 [38] and CIDECT [21] are quite conservative but unreliable. In addition, the predictions are quite dispersed. As a result, economical and reliable design equations are proposed in this study using the two design methods for predicting the resistances of cold-formed S900 steel grade CHS-to-RHS T- and X-joints at elevated temperatures ranging from 400°C to 1000°C.

Acknowledgement

The work described in this paper was fully supported by a grant from the Research Grants Council of the Hong Kong Special Administrative Region, China (Project No. 17210218).

References

[1] Pandey M, Chung KF and Young B. Design of cold-formed high strength steel tubular T-joints under compression loads. Thin-Walled Structures, 2021;164:107573.

[2] Pandey M and Young B. New Design Rules of Cold-formed High Strength Steel CHS-to-RHS X-Joints, Thin-Walled Structures, Elsevier (in press).

[3] Pandey M and Young B. High Strength Steel CHS-to-RHS T- and X-Joints: Performance and Design after Fire Exposures, Thin-Walled Structures, Elsevier (under review).

[4] Pandey M, Young B. Post-fire Mechanical Response of High Strength Steels. Thin-Walled Structures, 2021;164:107606.

[5] Pandey M and Young B. Post-Fire Behaviour of Cold-Formed High Strength Steel Tubular T- and X-Joints, Journal of Constructional Steel Research, 2021;186:106859.

[6] Pandey M and Young B. Static resistances of cold-formed high strength steel tubular non-90° X-Joints. Engineering Structures, 2021;239:112064.

[7] Pandey M and Young B. Ultimate Resistances of Member-Rotated Cold-Formed High Strength Steel Tubular T-Joints under Compression Loads, Engineering Structures, 2021;244:112601.

[8] Pandey M and Young B. Effect of Member Orientation on the Static Strengths of Cold-Formed High Strength Steel Tubular X-Joints, Thin-Walled Structures, 2022;170:108501.

[9] Pandey M and Young B. Stress Concentration Factors of Cold-Formed High Strength Steel Tubular T-Joints, Thin-Walled Structures, 2021;166:107996.

[10] Pandey M and Young B. Experimental Investigation on Stress Concentration Factors of Cold-formed High Strength Steel Tubular X-Joints, Engineering Structures, 2021;243:112408.

[11] Pandey M, Chung KF and Young B. Numerical investigation and design of fully chord supported tubular T-joints. Engineering Structures, 2021;239:112063.

[12] Lan X, Chan TM and Young B. Structural behaviour and design of high strength steel RHS X-joints. Engineering Structures, 2019; 200:109494.

[13] Lan X, Chan TM and Young B. Testing, finite element analysis and design of high strength steel RHS T-joints. Engineering Structures, 2021; 227:111184.

[14] Feng R. and Young B. Design of cold-formed stainless steel tubular joints at elevated temperatures. Engineering Structures, 2012;35:188-202.

[15] Chen J, Young B. Stress-strain curves for stainless steel at elevated temperatures. Engineering Structures, 2006;28(2):229–39.

[16] Dodaran NA, Ahmadi H, Lotfollahi-Yaghin MA. Static strength of axially loaded tubular KT-joints at elevated temperatures: study of geometrical effects and parametric formulation, Marine Structures, 2018;61:282–308.

[17] Shao Y, Haicheng Z, Dongping Y. Discussion on two methods for determining static strength of tubular T-joints at elevated temperature, Advances in Structural Engneering, 2017;20 (5):704–721.

[18] Nassiraei H, Lotfollahi-Yaghin MA, Neshaei SA, Zhu L. Structural behavior of tubular X-joints strengthened with collar plate under axially compressive load at elevated temperatures, Marine Structures, 2018;61:46–61.

[19] Lan X and Huang Y. Structural design of cold-formed stainless steel tubular X-and T-joints at elevated temperatures. Thin-Walled Structures, 2016;108:270-279.

[20] Lan X, Huang Y, Chan TM and Young B. Static strength of stainless steel K-and N-joints at elevated temperatures. Thin-Walled Structures, 2018;122:501-509.

[21] Packer JA, Wardenier J, Zhao XL, Vegte GJ van der, Kurobane Y. Design guide for rectangular hollow section (RHS) joints under predominantly static loading. Comite´ International pour le Developpement et l'Etude de la Construction TuECbulaire (CIDECT), Design Guide No. 3,

2nd edn., LSS Verlag, Dortmund, Germany, 2009.
[22] Gao F, Guan XQ, Zhu HP, Liu XN. Fire resistance behaviour of tubular T-joints reinforced with collar plates. Journal of Constructional Steel Research, 2015;115:106–120.
[23] Gao F, Zhu H, Liang H, Tian Y. Post-fire residual strength of steel tubular T-joint with concrete-filled chord. Journal of Constructional Steel Research, 2017;139:327–338.
[24] Cheng C, Shao Y, Yang J. Experimental and numerical study on fire resistance of circular tubular T-joints. Journal of Constructional Steel Research, 2013;85:24–39.
[25] Chen C, Shao YB, Yang J. Study on fire resistance of circular hollow section (CHS) T-joint stiffened with internal rings. Thin-Walled Structures, 2015;92:104–114.
[26] Ozyurt E, Wang YC and Tan KH. Elevated temperature resistance of welded tubular joints under axial load in the brace member. Engineering Structures, 2014;59:574-586.
[27] Ozyurt E and Wang YC. Resistance of axially loaded T-and X-joints of elliptical hollow sections at elevated temperatures–a finite element study. Structures, 2018;14:15-31.
[28] He S, Shao Y, Zhang H and Wang Q. Parametric study on performance of circular tubular K-joints at elevated temperature. Fire safety journal, 2015;71:174-186.
[29] Nguyen MP, Fung TC and Tan KH. An experimental study of structural behaviours of CHS T-joints subjected to brace axial compression in fire condition. Tubular Structures XIII, Hong Kong, 2010:725-732.
[30] Nguyen MP, Tan KH and Fung TC. Numerical models and parametric study on ultimate strength of CHS T-joints subjected to brace axial compression under fire condition. Tubular Structures XIII, Hong Kong, 2010:733-740.
[31] Yu W, Zhao J, Luo H, Shi J and Zhang D. Experimental study on mechanical behavior of an impacted steel tubular T-joint in fire. Journal of Constructional Steel Research, 2011; 67(9):1376-1385.
[32] Jin M, Zhao J, Chang J and Zhang D. Experimental and parametric study on the post-fire behavior of tubular T-joint. Journal of Constructional Steel Research, 2012;70:93-100.
[33] Liu M, Zhao J and Jin M. An experimental study of the mechanical behavior of steel planar tubular trusses in a fire. Journal of Constructional Steel Research, 2010;66(4):504-511.
[34] Yu W, Zhao J, Luo H, Shi J and Zhang D. Experimental study on mechanical behavior of an impacted steel tubular T-joint in fire. Journal of Constructional Steel Research, 2011;67(9):1376-1385.
[35] Xu J, Zhao J, Song Z and Liu M. Prediction of ultimate bearing capacity of Tubular T-joint under fire using artificial neural networks. Safety science, 2012;50(7):1495-1501.
[36] Tan KH, Fung TC and Nguyen MP. Structural behavior of CHS T-Joints subjected to brace axial compression in fire conditions. Journal of Structural Engineering, 2013;139(1):73-84.
[37] Fung TC, Tan KH and Nguyen MP. Structural behavior of CHS T-joints subjected to static in-plane bending in fire conditions. Journal of Structural Engineering, 2016;142(3):04015155.
[38] Eurocode 3 (EC3), Design of Steel Structures-Part 1-8: Design of Joints, EN 1993-1-8, European Committee for Standardization, CEN, Brussels, Belgium, 2005.
[39] Abaqus/Standard. Version 6.17. USA: K. a. S. Hibbit; 2017.
[40] Ozyurt E and Wang YC. A numerical investigation of static resistance of welded planar steel tubular joints under in-plane and out-of-plane bending at elevated temperatures. Engineering Structures, 2019;199:109622.
[41] Nassiraei H, Mojtahedi A, Lotfollahi-Yaghin MA and Zhu L. Capacity of tubular X-joints reinforced with collar plates under tensile brace loading at elevated temperatures. Thin-Walled Structures, 2019;142:426-443.
[42] Azari-Dodaran N, Ahmadi H, Zhu L and Li P. Experimental and numerical study of the ultimate

load for collar-plate-reinforced tubular K-joints at fire-induced elevated temperatures. Ships and Offshore Structures, 2022;17(5):1159-1177.
[43] Ozyurt E. Finite element study on axially loaded reinforced Square Hollow Section T-joints at elevated temperatures. Thin-Walled Structures, 2020;148:106582.
[44] Lan X, Wang F, Luo Z, Liu D, Ning C and Xu X. Joint strength reduction factor of internally ring-stiffened tubular joints at elevated temperatures. Advances in Structural Engineering, 2016;19(10):1650-1660.
[45] Azari-Dodaran N and Ahmadi H. Numerical study on the ultimate load of offshore two-planar tubular KK-joints at fire-induced elevated temperatures. Journal of Marine Engineering & Technology, 2022;21(4):205-233.
[46] Dodaran NA, Ahmadi H and Lotfollahi-Yaghin MA. Parametric study on structural behavior of tubular K-joints under axial loading at fire-induced elevated temperatures. Thin-Walled Structures, 2018; 130:467-486.
[47] Ozyurt E and Wang YC. Resistance of T- and K-joints to tubular members at elevated temperatures. In Proc of Applications of Structural Fire Engineering, Wald, Burgess, Horova, Jana, Jirku (eds), CTU Publishing House, Prague, 2013:179-185.
[48] Ozyurt E and Wang YC. Resistance of welded tubular T-and X-joints made of high strength steel at elevated temperatures. In Proceedings of the 17th international symposium on tubular structures, 2019:9-12.
[49] Azari-Dodaran N and Ahmadi H. Static behavior of offshore two-planar tubular KT-joints under axial loading at fire-induced elevated temperatures. Journal of Ocean Engineering and Science, 2019;4(4):352-372.
[50] Wang YC and Ozyurt E. Static resistance of axially loaded multiplanar gap KK-joints of Circular Hollow sections at elevated temperatures. Engineering Structures, 2021; 229:111676.
[51] Nassiraei H. Static strength of tubular T/Y-joints reinforced with collar plates at fire induced elevated temperature. Marine Structures, 2019;67:102635.
[52] Azari-Dodaran N and Ahmadi H. Structural behavior of right-angle two-planar tubular TT-joints subjected to axial loadings at fire-induced elevated temperatures. Fire Safety Journal, 2019;108:102849.
[53] Li HT and Young B. Cold-formed high strength steel SHS and RHS beams at elevated temperatures. Journal of Constructional Steel Research, 2019;158:475-485.
[54] Li HT and Young B. Material properties of cold-formed high strength steel at elevated temperatures. Thin-Walled Structures, 2017;115:289-299.
[55] Pandey M and Young B. Tests of cold-formed high strength steel tubular T-joints. Thin-Walled Structures, 2019;143:106200.
[56] Pandey M and Young B. Structural performance of cold-formed high strength steel tubular X-Joints under brace axial compression. Engineering Structures, 2020;208:109768.
[57] ISO-834. Fire-resistance tests-Elements of Building Construction-Part 1-General requirements. ISO 834-1, International Organization of Standards, 1999.
[58] Crockett P. Finite element analysis of welded tubular connections. PhD Thesis, University of Nottingham, 1994.
[59] Ma JL, Chan TM and Young B. Design of cold-formed high strength steel tubular beams. Engineering Structures, 2017;151:432-443.
[60] Li QY and Young B. Design of cold-formed steel built-up open section members under combined compression and bending. Thin-Walled Structures, 2022;172:108890.
[61] Li HT and Young B. Cold-formed stainless steel RHS members undergoing combined bending and web crippling: Testing, modelling and design. Engineering Structures, 2022;250:113466.

[62] SSAB. Strenx Tube 900 MH. Data Sheet 2042, Sweden, 2017.
[63] EN 10219-2. Cold formed welded structural hollow sections of non-alloy and fine grain steels- Part 2: Tolerances, dimensions and sectional properties. European Committee for Standardization (CEN), Brussels, Belgium; 2006.
[64] AWS D1.1/D1.1M, Structural Welding Code – Steel, American Welding Society (AWS), Miami, USA, 2020.
[65] Eurocode 3 (EC3), Design of steel structures. Part 1-12: Additional rules for the extension of EN 1993 up to steel grades S700, EN 1993-1-12, European Committee for Standardization, CEN, Brussels, Belgium, 2007.
[66] IIW Doc. XV-1402-12 and IIW Doc. XV-E-12-433. Static design procedure for welded hollow section joints – Recommendations. International Institute of Welding, Paris, France, 2012.
[67] AISI S100. North American Specification for the design of cold-formed steel structural members. American Iron and Steel Institute (AISI), Washington, D.C., USA, 2016.

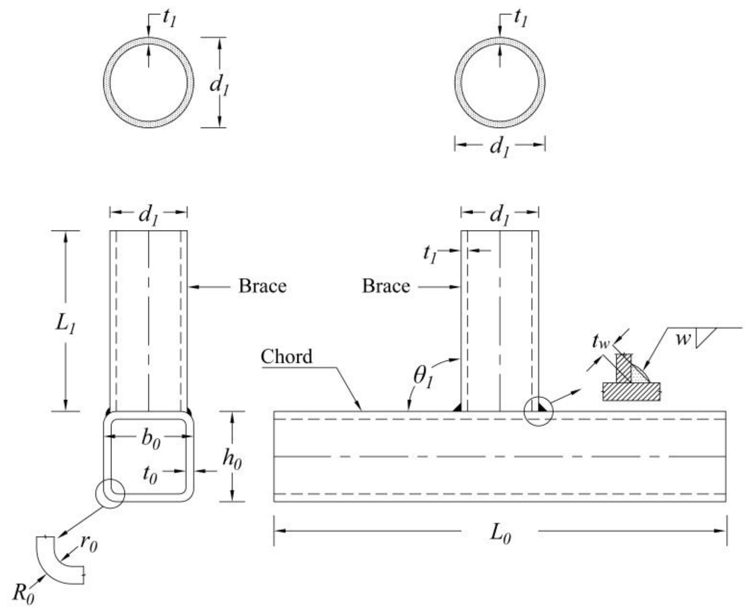

Fig. 1. Representations of geometric notations for CHS-to-RHS T-joint (also valid for X-joint).

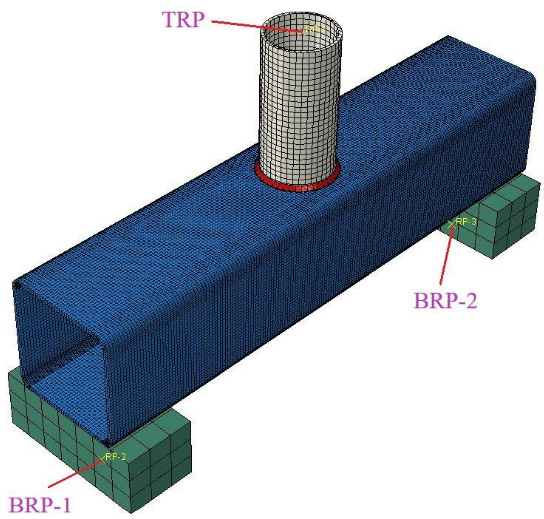

(a) Typical FE model of CHS-to-RHS T-joint with small β value (β=0.59).

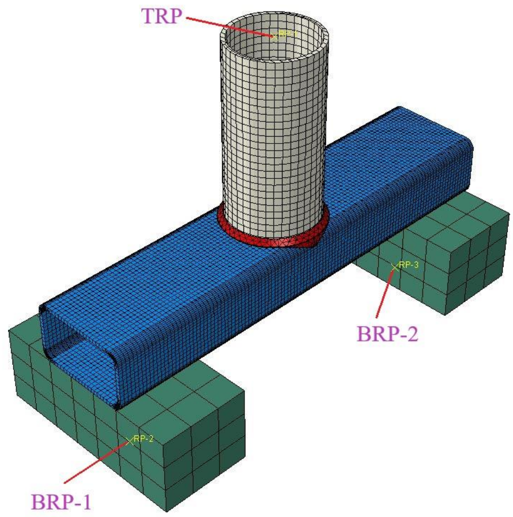

(b) Typical FE model of CHS-to-RHS T-joint with large β value (β=0.89).

Fig. 2. Typical FE models of CHS-to-RHS T-joints.

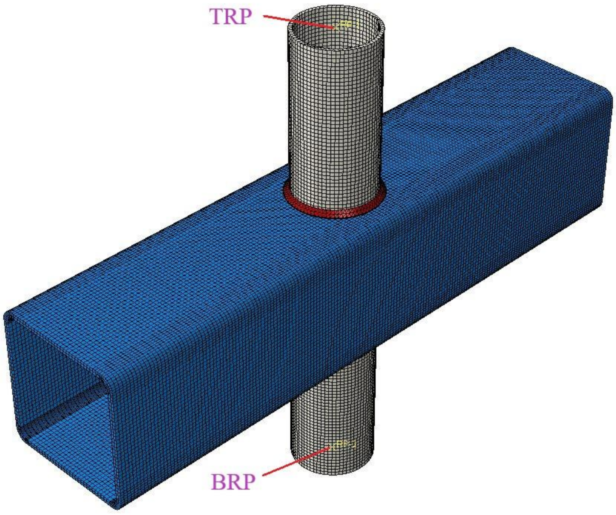

(a) Typical FE model of CHS-to-RHS X-joint with small β value (β=0.59).

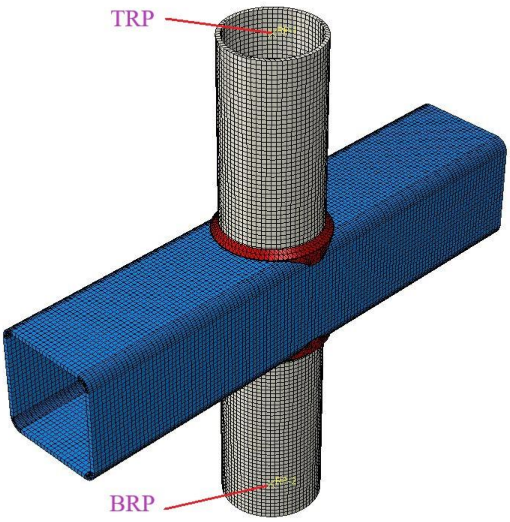

(b) Typical FE model of CHS-to-RHS X-joint with large β value (β=0.89).

Fig. 3. Typical FE models of CHS-to-RHS X-joints.

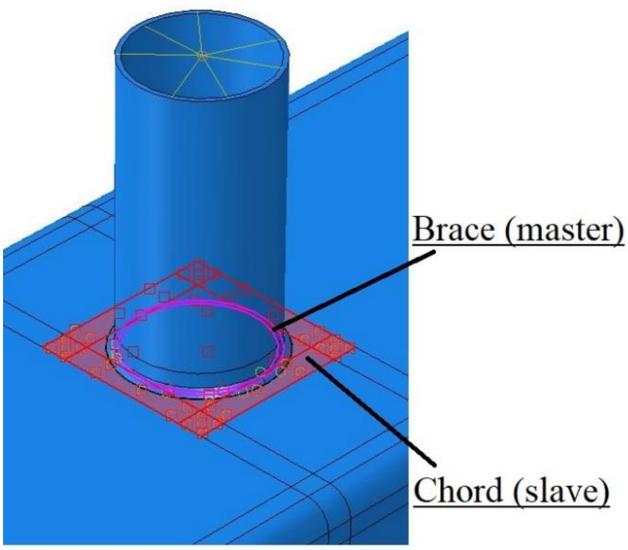

(a) Brace-to-chord contact interaction in CHS-to-RHS T- and X-joints.

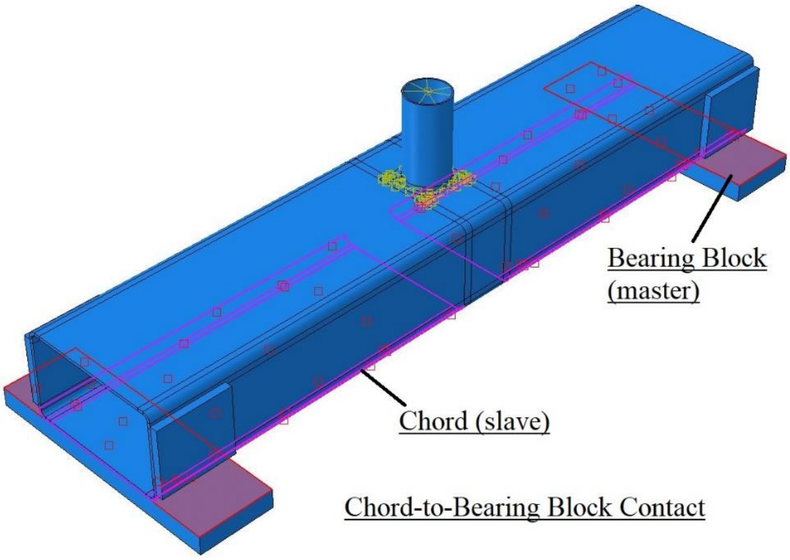

(b) Chord-to-bearing block contact interaction in CHS-to-RHS T-joint.

Fig. 4. Typical contact interactions used in CHS-to-RHS T- and X-joints.

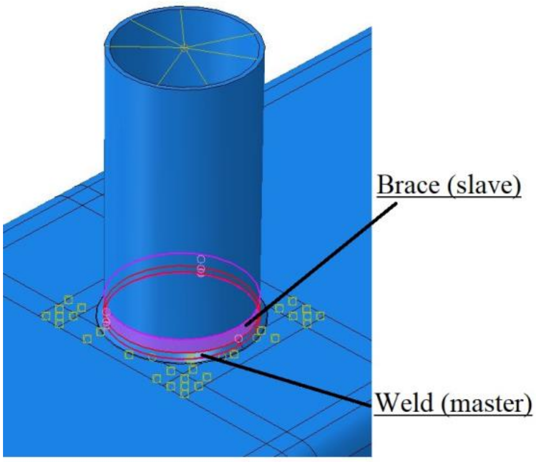

(a) Weld-to-brace tie connection in CHS-to-RHS T- and X-joints.

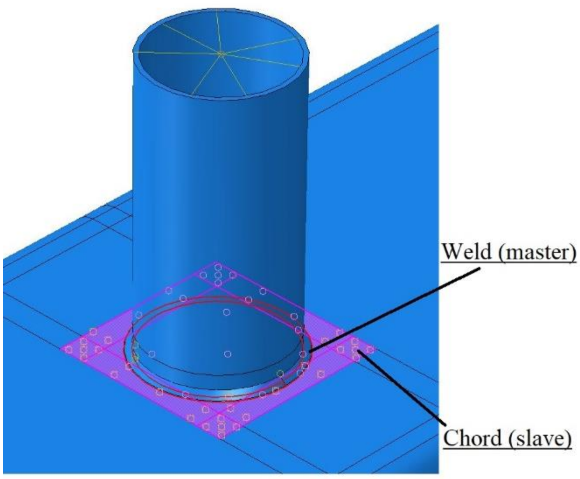

(b) Weld-to-chord tie connection in CHS-to-RHS T- and X-joints.

Fig. 5. Typical tie connections used in CHS-to-RHS T- and X-joints.

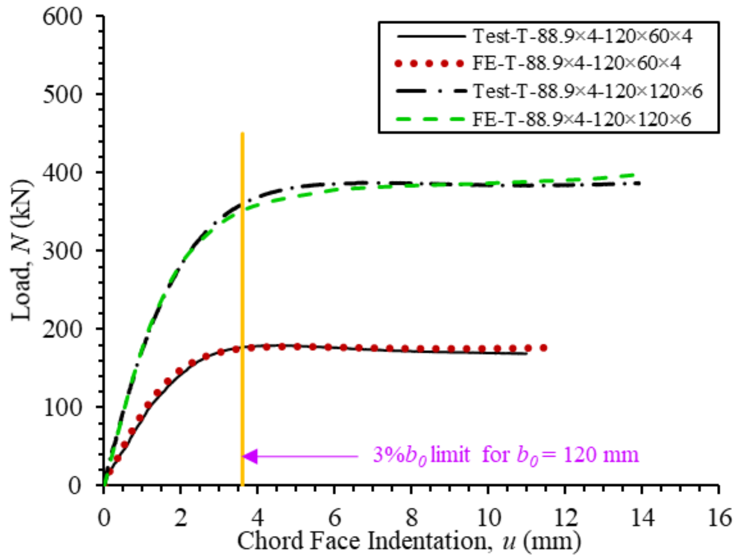

(a) Load vs chord face indentation curves.

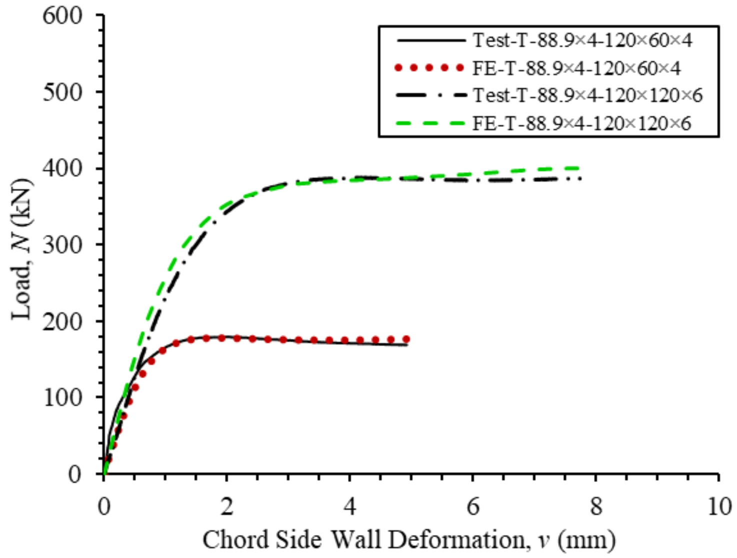

(b) Load vs chord side wall deformation curves.

Fig. 6. Test vs FE load-deformation curves for CHS-to-RHS T-joints at ambient temperature.

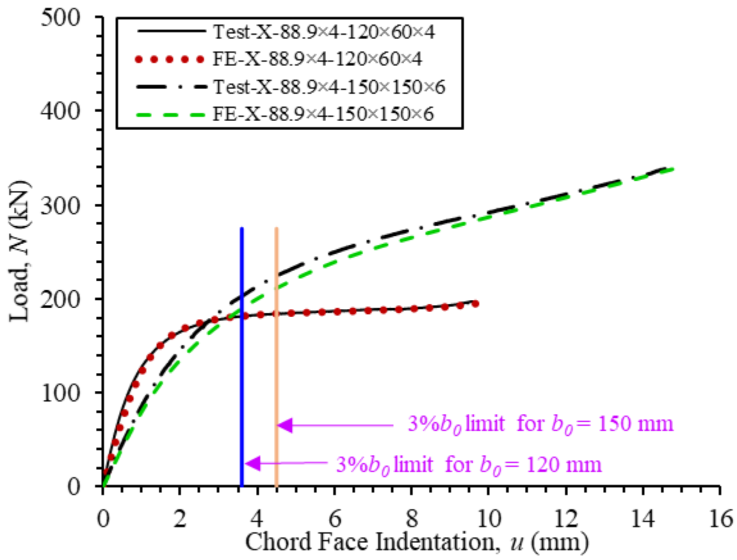

(a) Load vs chord face indentation curves.

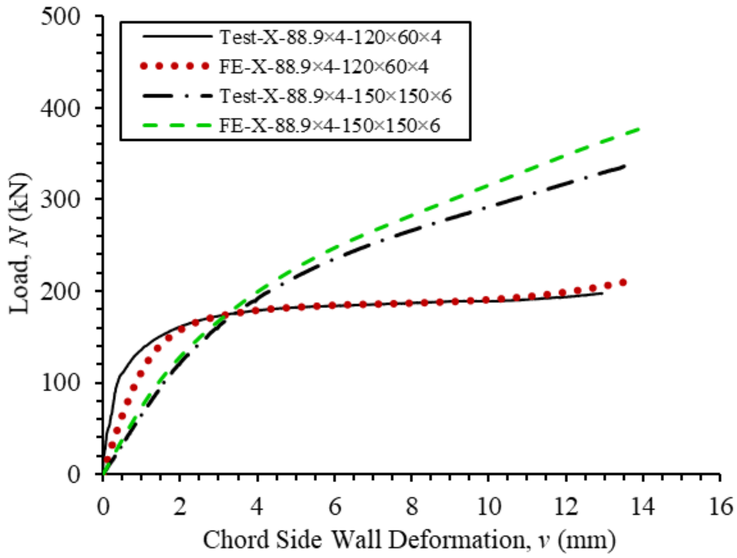

(b) Load vs chord side wall deformation curves.

Fig. 7. Test vs FE load-deformation curves for CHS-to-RHS X-joints at ambient temperature.

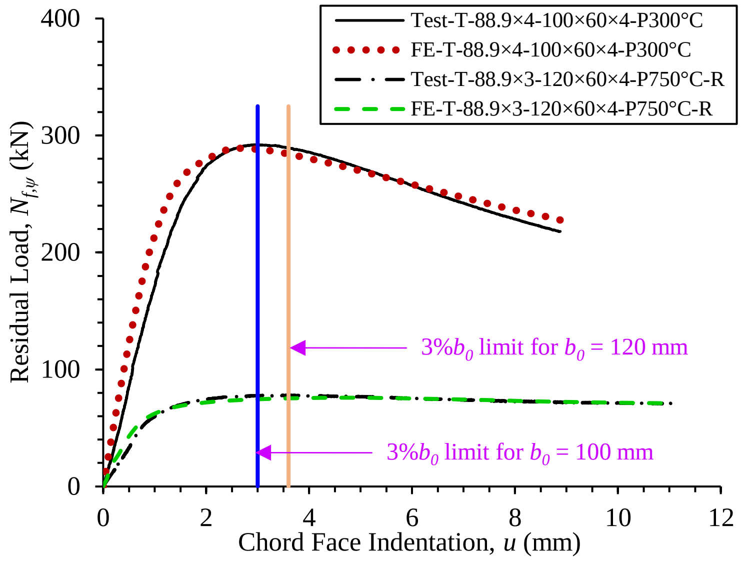

(a) Residual Load vs chord face indentation curves.

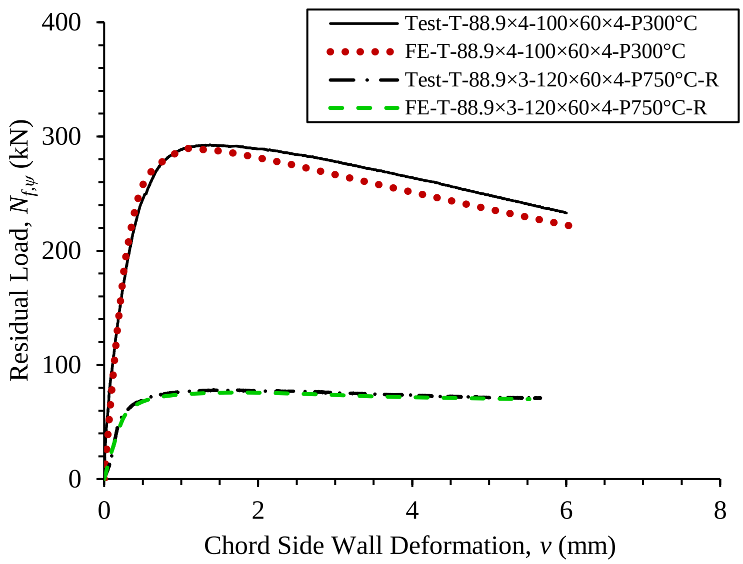

(b) Residual Load vs chord side wall deformation curves.

Fig. 8. Test vs FE load-deformation curves for CHS-to-RHS T-joints for post-fire conditions.

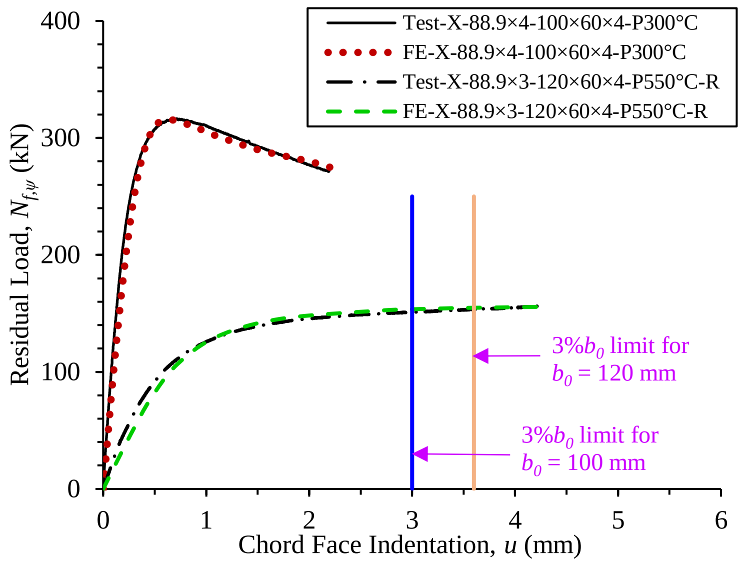

(a) Residual Load vs chord face indentation curves.

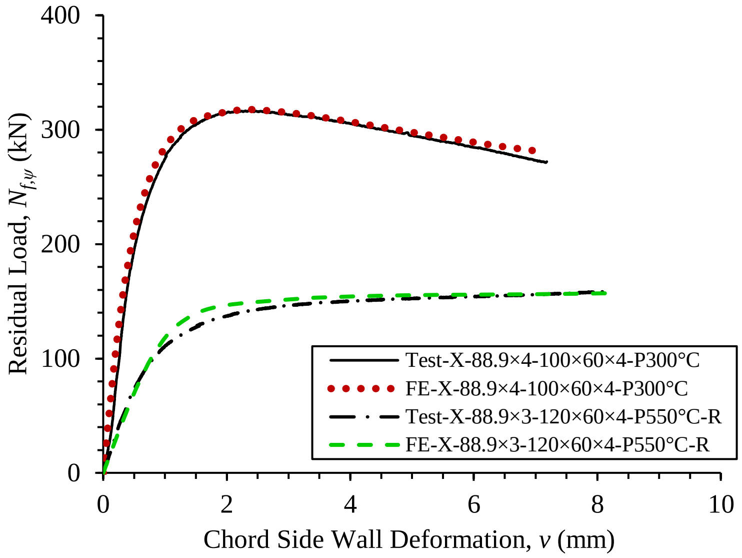

(b) Residual Load vs chord side wall deformation curves.

Fig. 9. Test vs FE load-deformation curves for CHS-to-RHS X-joints for post-fire conditions.

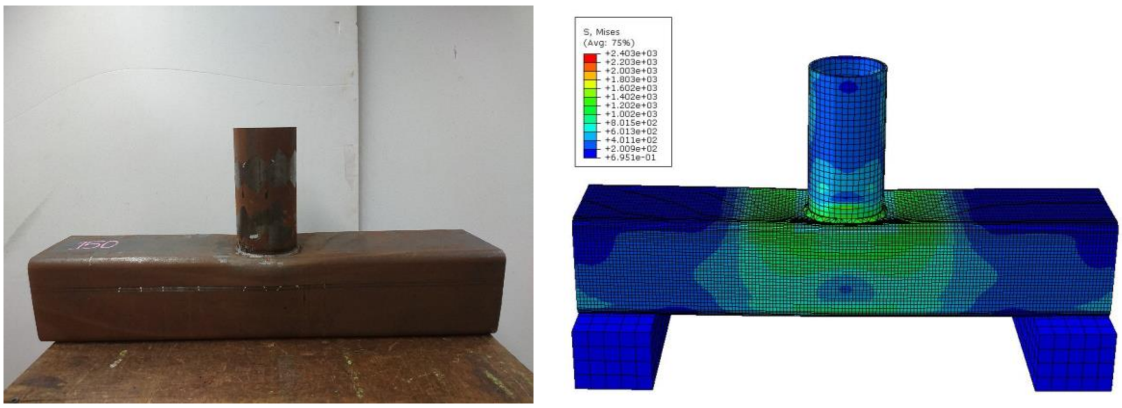

(a) Test vs FE comparison for CHS-to-RHS T-joint failed by F mode at ambient temperature.

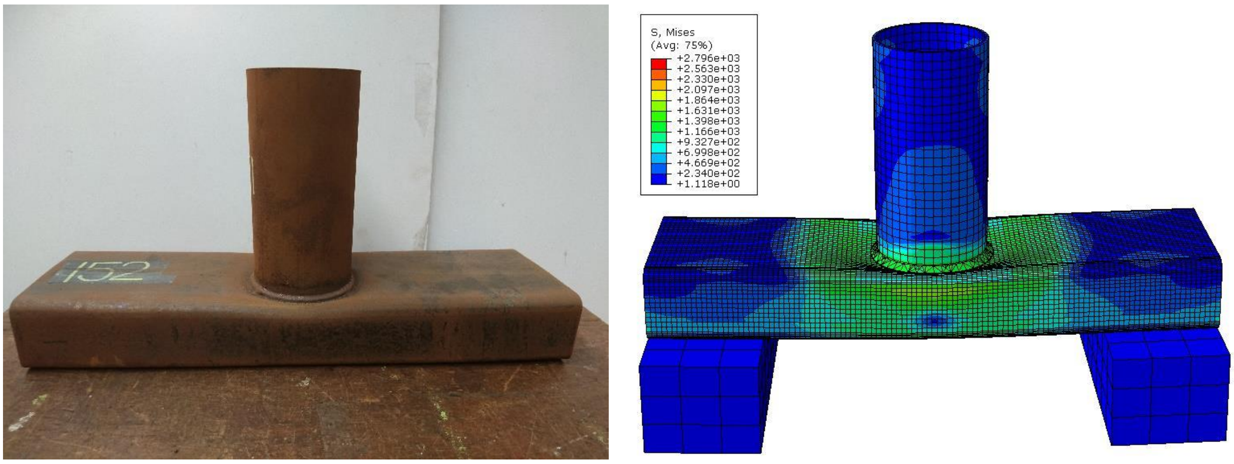

(b) Test vs FE comparison for CHS-to-RHS T-joint failed by F+S mode at ambient temperature.

Fig. 10. Test vs FE comparisons of failure modes for CHS-to-RHS T-joints at ambient temperature.

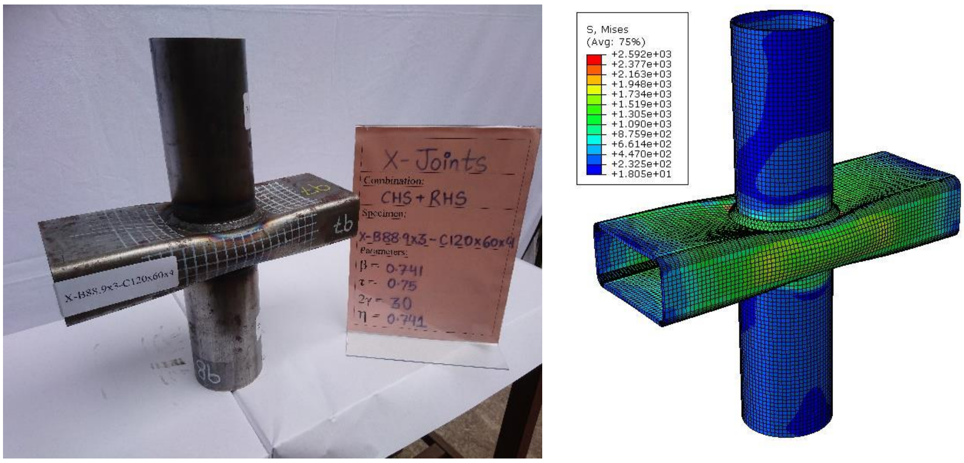

(a) Test vs FE comparison for CHS-to-RHS X-joint failed by F mode at ambient temperature.

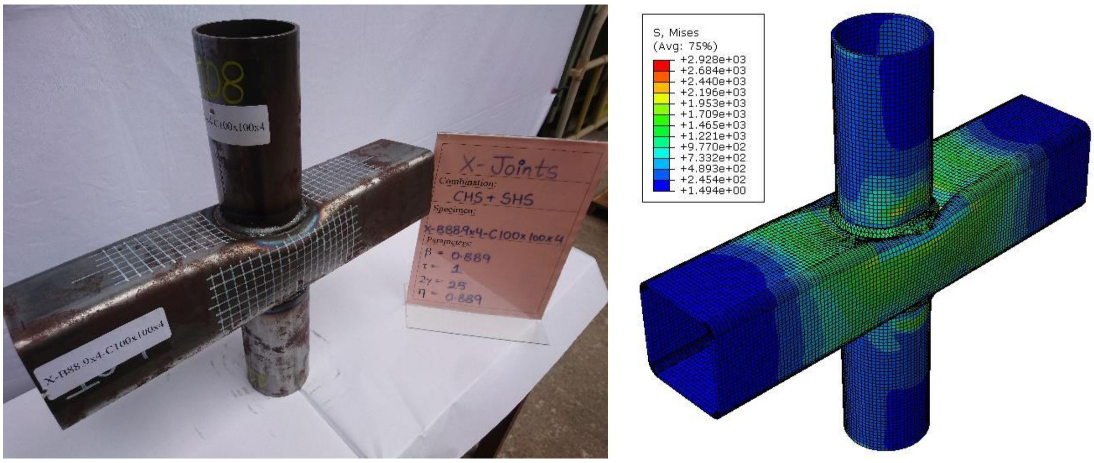

(b) Test vs FE comparison for CHS-to-RHS X-joint failed by F+S mode at ambient temperature.

Fig. 11. Test vs FE comparisons of failure modes for CHS-to-RHS X-joints at ambient temperature.

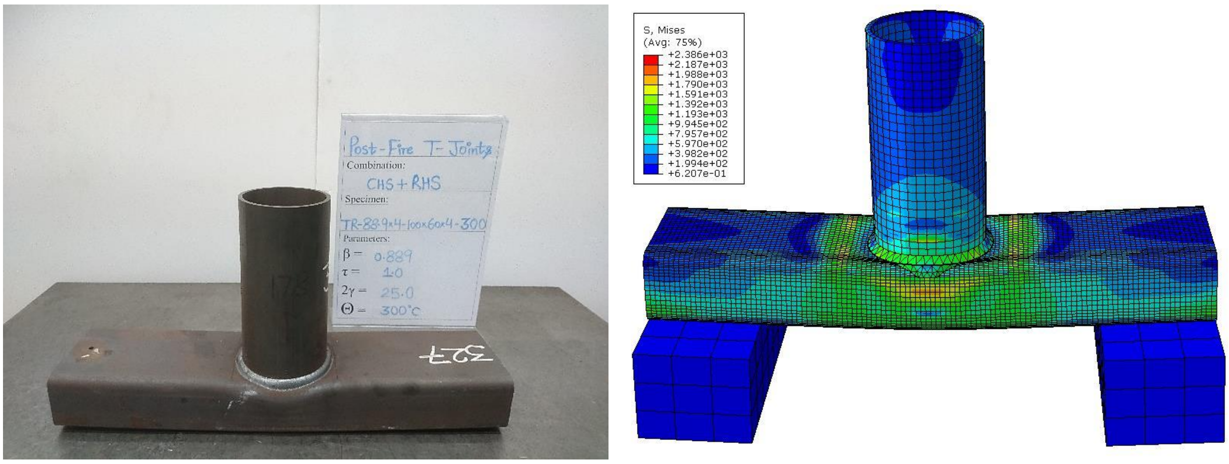

(a) Test vs FE comparison for CHS-to-RHS T-joint failed by F mode for post-fire conditions.

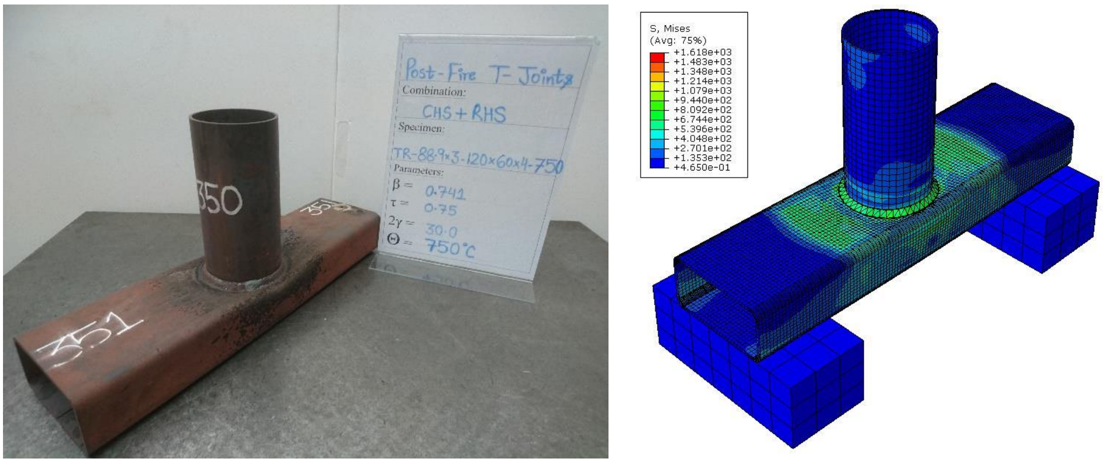

(b) Test vs FE comparison for CHS-to-RHS T-joint failed by F+S mode for post-fire conditions.

Fig. 12. Test vs FE comparisons of failure modes for CHS-to-RHS T-joints for post-fire conditions.

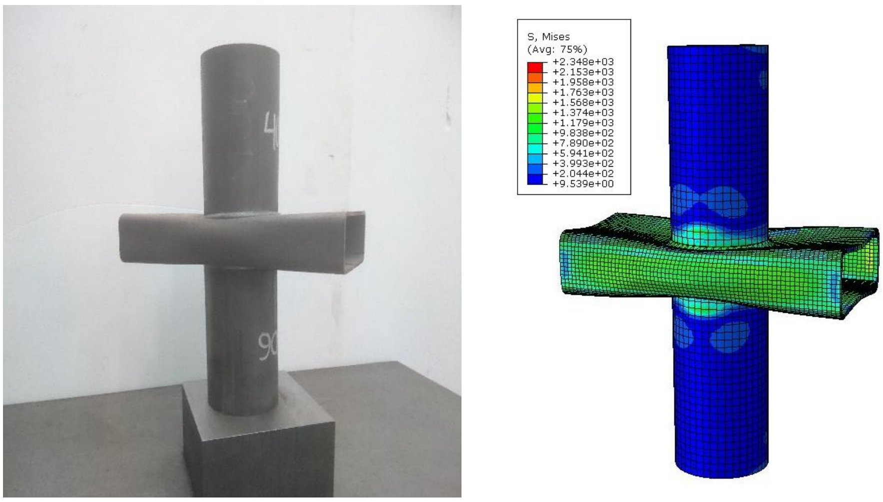

(a) Test vs FE comparison for CHS-to-RHS X-joint failed by F mode for post-fire conditions.

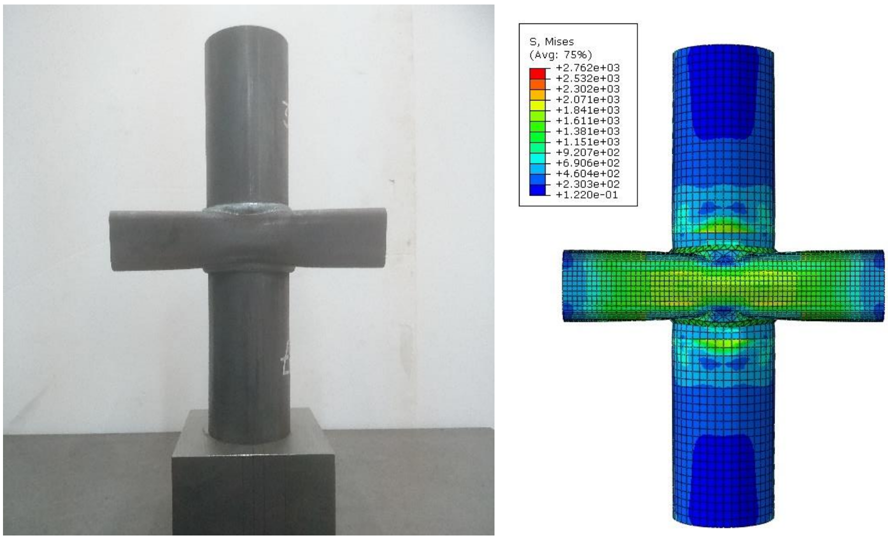

(b) Test vs FE comparison for CHS-to-RHS X-joint failed by F+S mode for post-fire conditions.

Fig. 13. Test vs FE comparisons of failure modes for CHS-to-RHS X-joints for post-fire conditions.

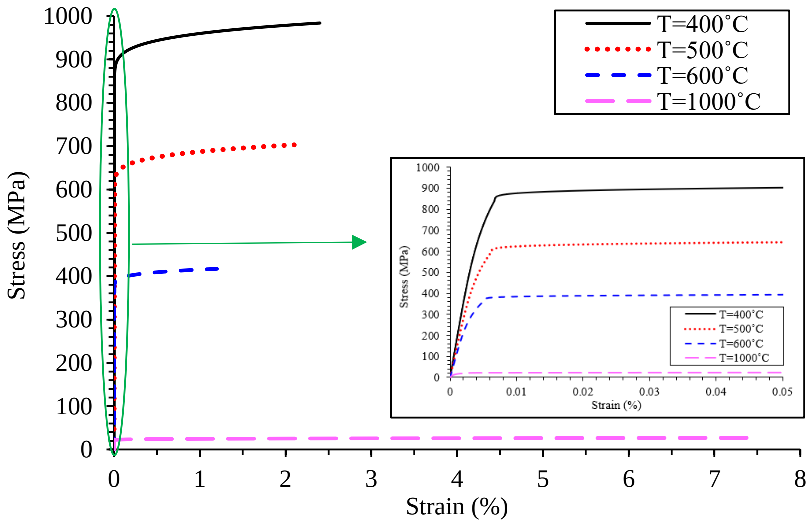

Fig. 14. Stress-strain curves at elevated temperatures [53].

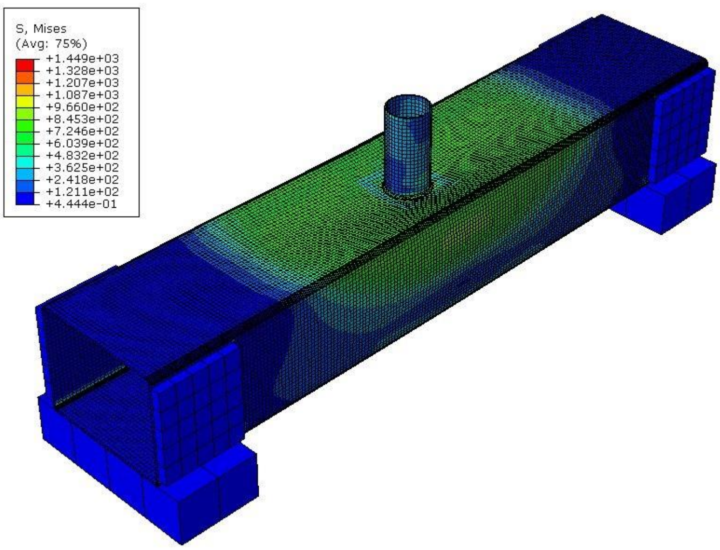

(a) CHS-to-RHS T-joint failed by F mode at elevated temperature.

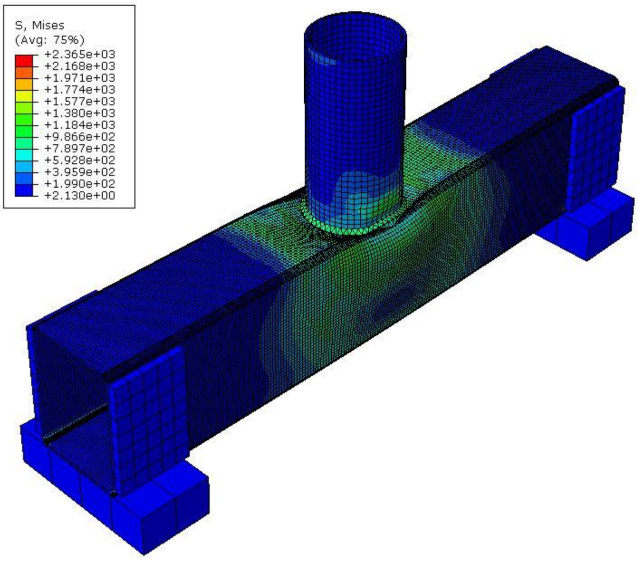

(b) CHS-to-RHS T-joint failed by F+S mode at elevated temperature.

Fig. 15. CHS-to-RHS T-joints failed by F and F+S modes at elevated temperature (500°C).

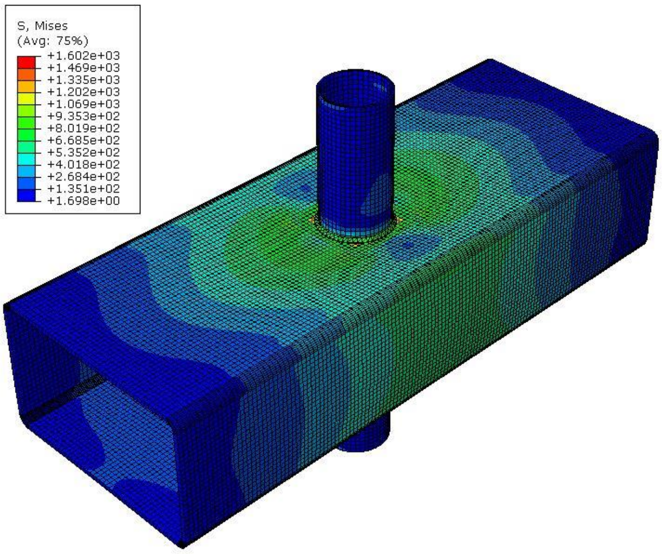

(a) CHS-to-RHS X-joint failed by F mode at elevated temperature.

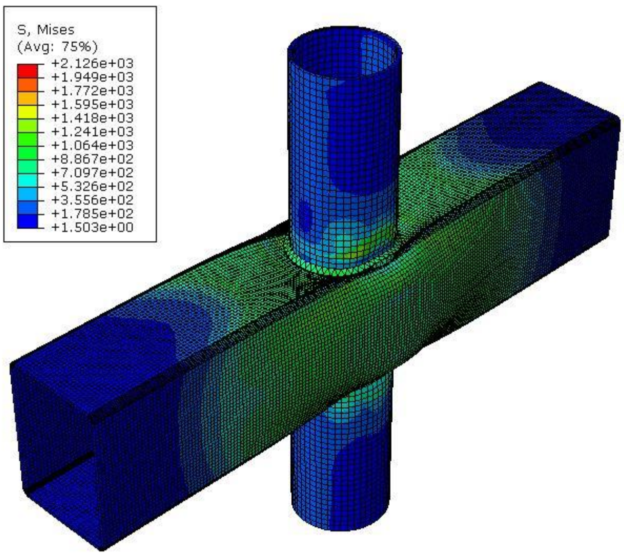

(b) CHS-to-RHS X-joint failed by F+S mode at elevated temperature.

Fig. 16. CHS-to-RHS X-joints failed by F and F+S modes at elevated temperature (500°C).

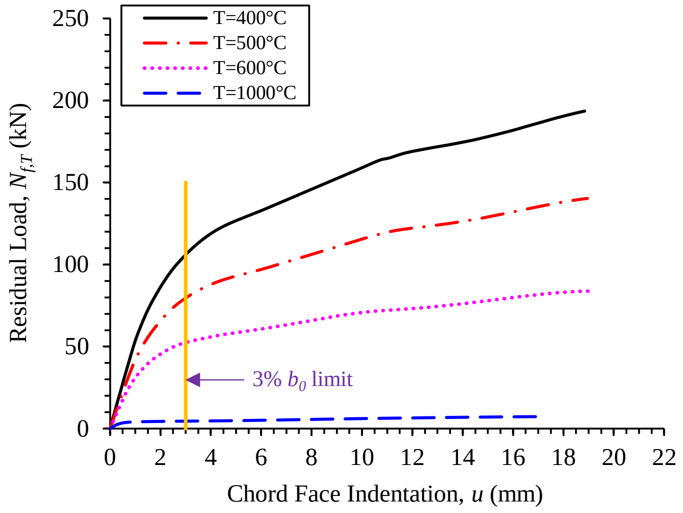

(a) Variations of load vs deformation curves for typical CHS-to-RHS T-joint (T-30×3-100×100×6; β=0.30) failed by F mode at elevated temperatures.

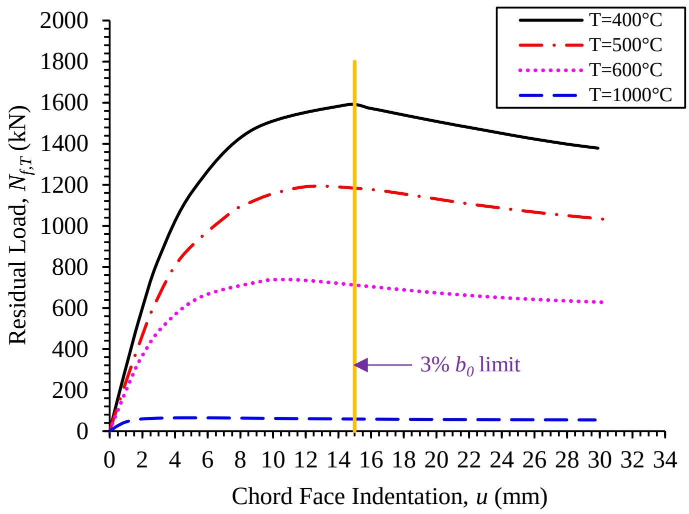

(b) Variations of load vs deformation curves for typical CHS-to-RHS T-joint (T-450×10-500×500×10; β=0.90) failed by F+S mode at elevated temperatures.

Fig. 17. Variations of load vs deformation curves for typical CHS-to-RHS T-joints at elevated temperatures.

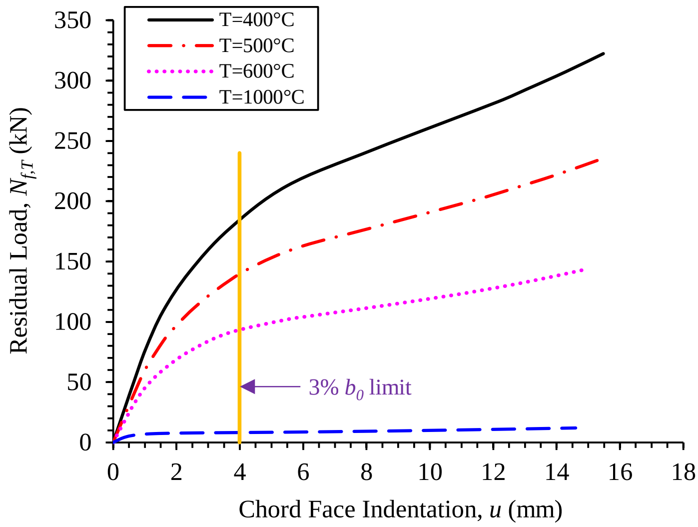

(a) Variations of load vs deformation curves for typical CHS-to-RHS X-joint (X-40×4-133×240×8;

β=0.30) failed by F mode at elevated temperatures.

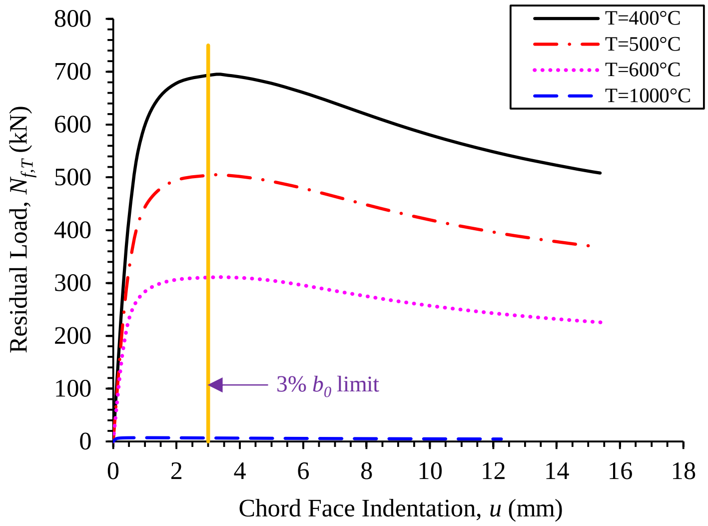

(b) Variations of load vs deformation curves for typical CHS-to-RHS X-joint (X-90×6-100×100×6; β=0.90) failed by F+S mode at elevated temperatures.

Fig. 18. Variations of load vs deformation curves for typical CHS-to-RHS X-joints at elevated temperatures.

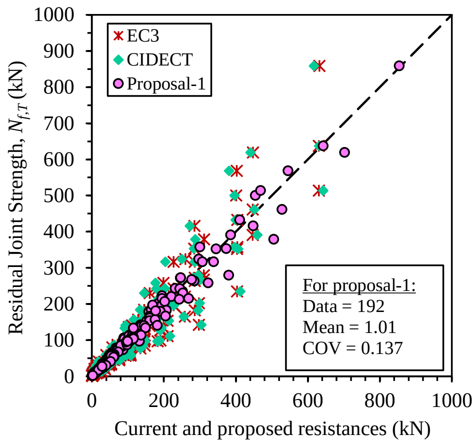

(a) For Proposal-1.

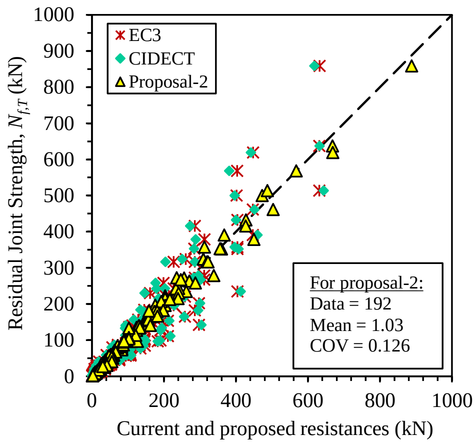

(b) For Proposal-2.

Fig. 19. Comparisons of joint resistances at elevated temperatures with current and proposed nominal resistances for CHS-to-RHS T-joints failed by F mode.

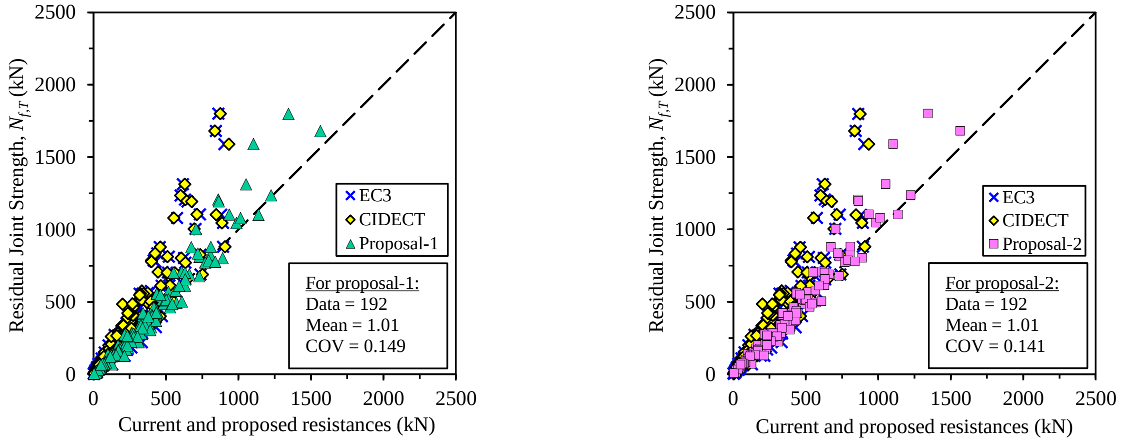

(a) For Proposal-1. (b) For Proposal-2.

Fig. 20. Comparisons of joint resistances at elevated temperatures with current and proposed nominal resistances for CHS-to-RHS T-joints failed by F+S mode.

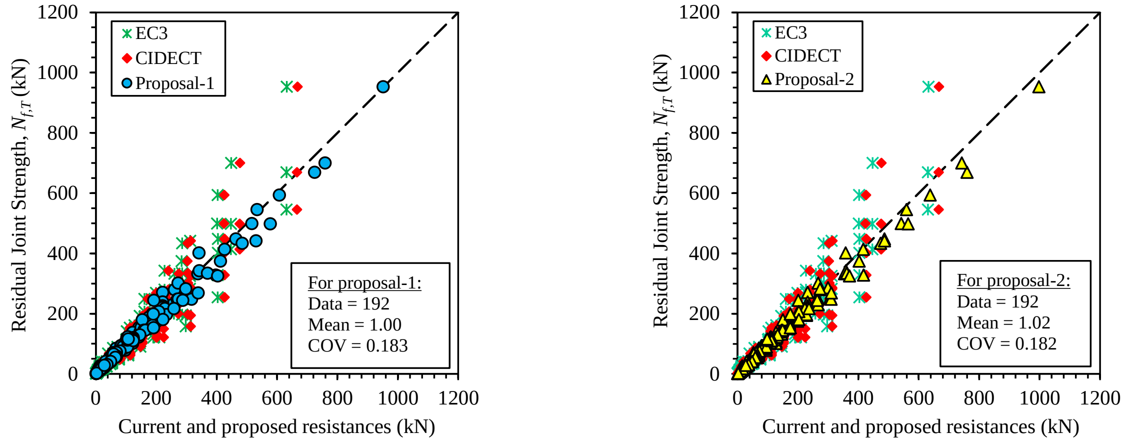

(a) For Proposal-1. (b) For Proposal-2.

Fig. 21. Comparisons of joint resistances at elevated temperatures with current and proposed nominal resistances for CHS-to-RHS X-joints failed by F mode.

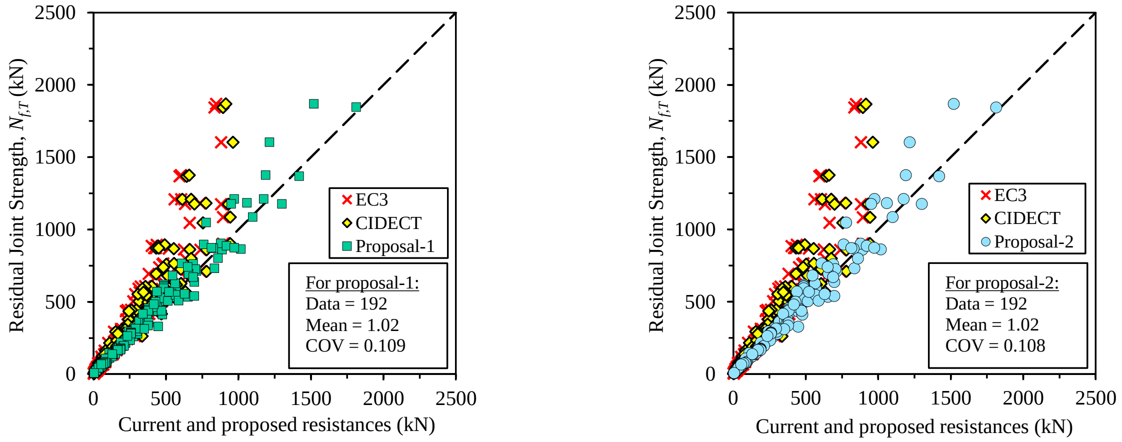

(a) For Proposal-1. (b) For Proposal-2.

Fig. 22. Comparisons of joint resistances at elevated temperatures with current and proposed nominal resistances for CHS-to-RHS X-joints failed by F+S mode.

Table 1. Mechanical properties at elevated temperatures [53].

Temperatures (°C)	Nominal Yield Strengths (MPa)	Mechanical properties at elevated temperatures				
		E_0 (GPa)	$\sigma_{0.2}$ (MPa)	σ_u (MPa)	$0.80\sigma_u$ (MPa)	ε_u (%)
21	900	207	1024	1181	945	2.4
400	900	179	839	984	787	2.4
500	900	143	594	703	562	2.1
600	900	114	368	417	334	1.2
1000	900	30	21	27	22	7.4

Table 2. Overall ranges of critical parameters used in parametric study.

Parameters	Validity Ranges
T	[400°C to 1000°C]
β (d_1/b_0)	[0.30 to 0.90]
2γ (b_0/t_0)	[16.6 to 50]
h_0/t_0	[16.6 to 50]
τ (t_1/t_0)	[0.50 to 1.0]

Table 3. Summary of comparisons between joint resistances at elevated temperatures with existing and proposed nominal resistances for CHS-to-RHS T-joints failed by F mode.

Elevated Temperatures (T)	Parameters	Comparisons			
		$\frac{N_{f,T}}{N_{E,T}}$	$\frac{N_{f,T}}{N_{C,T}}$	$\frac{N_{f,T}}{N_{pn1}}$	$\frac{N_{f,T}}{N_{pn2}}$
400°C	No. of data (n)	48	48	48	48
	Mean (P_m)	0.86	0.89	1.06	1.02
	COV (V_p)	0.302	0.321	0.071	0.071
500°C	No. of data (n)	48	48	48	48
	Mean (P_m)	0.91	0.94	0.98	1.03
	COV (V_p)	0.285	0.304	0.083	0.083
600°C	No. of data (n)	48	48	48	48
	Mean (P_m)	0.89	0.98	0.94	1.06
	COV (V_p)	0.222	0.252	0.114	0.114
1000°C	No. of data (n)	48	48	48	48
	Mean (P_m)	1.64	1.80	1.05	1.01

	COV (V_p)	0.273	0.299	0.199	0.199
Overall	No. of data (n)	192	192	192	192
	Mean (P_m)	1.08	1.15	1.01	1.03
	COV (V_p)	0.415	0.449	0.137	0.126
	Resistance factor (ϕ)	1.00	1.00	0.80	0.80
	Reliability index (β_0)	1.13	1.26	2.58	2.70

Table 4. Summary of comparisons between joint resistances at elevated temperatures with existing and proposed nominal resistances for CHS-to-RHS T-joints failed by F+S mode.

Elevated Temperatures (T)	Parameters	Comparisons			
		$\frac{N_{f,T}}{N_{E,T}}$	$\frac{N_{f,T}}{N_{C,T}}$	$\frac{N_{f,T}}{N_{pn1}}$	$\frac{N_{f,T}}{N_{pn2}}$
400°C	No. of data (n)	48	48	48	48
	Mean (P_m)	1.29	1.38	1.10	0.98
	COV (V_p)	0.278	0.273	0.132	0.132
500°C	No. of data (n)	48	48	48	48
	Mean (P_m)	1.30	1.37	1.01	0.99
	COV (V_p)	0.287	0.263	0.139	0.139
600°C	No. of data (n)	48	48	48	48
	Mean (P_m)	1.18	1.33	0.94	1.02
	COV (V_p)	0.255	0.247	0.135	0.135
1000°C	No. of data (n)	48	48	48	48
	Mean (P_m)	1.51	1.72	0.98	1.05
	COV (V_p)	0.191	0.183	0.150	0.150
Overall	No. of data (n)	192	192	192	192
	Mean (P_m)	1.32	1.45	1.01	1.01
	COV (V_p)	0.266	0.261	0.149	0.141
	Resistance factor (ϕ)	1.00	1.00	0.80	0.80
	Reliability index (β_0)	2.04	2.43	2.53	2.58

Table 5. Summary of comparisons between joint resistances at elevated temperatures with existing and proposed nominal resistances for CHS-to-RHS X-joints failed by F mode.

Elevated Temperatures (T)	Parameters	Comparisons			
		$\frac{N_{f,T}}{N_{E,T}}$	$\frac{N_{f,T}}{N_{C,T}}$	$\frac{N_{f,T}}{N_{pn1}}$	$\frac{N_{f,T}}{N_{pn2}}$
400°C	No. of data (n)	48	48	48	48
	Mean (P_m)	0.95	0.90	1.03	0.98
	COV (V_p)	0.277	0.277	0.161	0.161

500°C	No. of data (n)	48	48	48	48
	Mean (P_m)	1.01	0.95	0.98	1.00
	COV (V_p)	0.264	0.264	0.161	0.161
600°C	No. of data (n)	48	48	48	48
	Mean (P_m)	0.98	0.97	0.96	1.04
	COV (V_p)	0.202	0.202	0.175	0.175
1000°C	No. of data (n)	48	48	48	48
	Mean (P_m)	1.50	1.50	1.04	1.04
	COV (V_p)	0.131	0.131	0.219	0.219
Overall	No. of data (n)	192	192	192	192
	Mean (P_m)	1.11	1.08	1.00	1.02
	COV (V_p)	0.293	0.307	0.183	0.182
	Resistance factor (ϕ)	1.00	1.00	0.75	0.75
	Reliability index (β_0)	1.48	1.47	2.56	2.62

Table 6. Summary of comparisons between joint resistances at elevated temperatures with existing and proposed nominal resistances for CHS-to-RHS X-joints failed by F+S mode.

Elevated Temperatures (T)	Parameters	Comparisons			
		$\frac{N_{f,T}}{N_{E,T}}$	$\frac{N_{f,T}}{N_{C,T}}$	$\frac{N_{f,T}}{N_{pn1}}$	$\frac{N_{f,T}}{N_{pn2}}$
400°C	No. of data (n)	48	48	48	48
	Mean (P_m)	1.43	1.33	1.10	0.97
	COV (V_p)	0.259	0.249	0.101	0.101
500°C	No. of data (n)	48	48	48	48
	Mean (P_m)	1.48	1.36	1.01	1.03
	COV (V_p)	0.253	0.244	0.099	0.099
600°C	No. of data (n)	48	48	48	48
	Mean (P_m)	1.32	1.28	0.96	1.01
	COV (V_p)	0.239	0.228	0.098	0.098
1000°C	No. of data (n)	48	48	48	48
	Mean (P_m)	1.68	1.63	1.00	1.11
	COV (V_p)	0.206	0.210	0.082	0.082
Overall	No. of data (n)	192	192	192	192
	Mean (P_m)	1.48	1.40	1.02	1.02
	COV (V_p)	0.253	0.250	0.109	0.108
	Resistance factor (ϕ)	1.00	1.00	0.85	0.85
	Reliability index (β_0)	2.41	2.38	2.53	2.53